Meshed DC microgrid hierarchical control: A differential flatness approach

Igyso Zafeiratou, Ionela Prodan, Laurent Lefèvre, Laurent Piétrac

Meshed DC microgrid hierarchical control: A differential flatness approach

Igyso Zafeiratou, Ionela Prodan, Laurent Lefèvre, Laurent Piétrac

Meshed DC microgrid hierarchical control: a differential flatness approach

I. Zafeiratou[a], I. Prodan[a], L. Lefèvre[a], L. Piétrac[b]

[a] *Univ. Grenoble Alpes, Grenoble INP* ☆, *LCIS, F-26000 Valence, France (e-mail: igyso.zafeiratou, ionela.prodan, laurent.lefevre@lcis.grenoble-inp.fr)*
[b] *Université de Lyon, CNRS, INSA-Lyon, a.m.PERE, F-69621 Villeurbanne, France (e-mail: laurent.pietrac@insa-lyon.fr)*

Abstract

In this paper, a meshed DC microgrid control architecture whose goal is to manage load balancing and efficient power distribution is introduced. A novel combination of port-Hamiltonian (PH) modeling with differential flatness and B-splines parametrization is introduced and shown to improve the microgrid's performance. A three layer supervision structure is considered: i) B-spline parametrized flat output provide continuous profiles for load balancing and price reduction (high level); ii) the profiles are tracked through a MPC implementation with stability guarantees (medium level); iii) explicit switching laws applied to the DC/DC converters ensure appropriate power injection. Each level functions at a different time-scale (from slow to fast), and the control laws are chosen appropriately. The effectiveness of the proposed approach is evaluated by simulations over a DC microgrid composed by a collection of solar panels (PV), an energy storage system (ES), a utility grid (UG) and a consumers' demand.

Keywords: DC microgrid; Meshed topology; Port-Hamiltonian systems; Differential flatness; Hierarchical control; Power balancing.

1. Introduction

The integration of renewable energy sources and energy storing elements into the electrical grid systems ensures the safe and reliable power distribution

☆ Institute of Engineering Univ. Grenoble Alpes

and establishes their existence into the grid operation support [24]. Despite the domination of AC transmission networks, the interest on DC microgrids has greatly grown as a result of the constant development and production of the DC equipment both for energy sources (e.g. solar panels, batteries) and loads (e.g. electrical vehicles, elevators and various smaller DC loads such as computers, LED lights, etc.). In general, many aspects must be considered in order to decide the appropriate structure of a microgrid, such as its topology [6], the distance among the sources and the loads as well as the amount of the sources and the type of the converters. A sufficient amount of storing elements is indispensable and depends on many factors such as the sizing of the batteries or their lifetime [14]. Considering all the above, several modeling and control methods have been developed through the years.

Modeling methodologies: In the literature, different modeling methodologies have been studied to describe such complex dynamical systems. For instance, the Takagi−Sugeno fuzzy modeling approach [45] describes linear models based on input/output datasets covering multiple operational conditions of the system. Furthermore, the multi−agent based modeling [17] comprises agents which are active entities, individual or collective, and represent a computer model. Using the multi−agent paradigm in a microgrid system, different types of agents can be employed: control agents for controlling the physical units of the system; management agents for managing the microgrid and taking decisions; ancillary agents for performing tasks such as communication and data storage [26]. The global dynamics of the system emerges from the interaction among them. Another classical way to model the microgrid components is by using differential equations [35], which gives an explicit representation of the system dynamics through constitutive equations (for resistors, batteries, capacitors, etc.) and balance equations (Kirchoff laws). However, through this model description, the power conservation property and the components' interconnections are not explicitly described. Such an approach is the PH formulation approach which applies for general multiphysical systems [36, 10]. It aims at providing an exhaustive, explicit and modular description of the power routing

through the network topology, together with the constitutive equations for the resistor−like, capacitor/inductor−like, transformers and sources components. Besides, the equations in a PH model may be generated in a straightforward way from its Bond Graph[1]. This approach to generate structured physically−based dynamical models for electrical grids has already been applied successfully in [39]. In this structural description, balance equations and energy properties of the systems (passivity, conservation) are satisfied independently by the specific constitutive equations and the numerical values of the model parameters. The overall interconnection structure topology and balance equations are summarized in a geometrical linear structure (namely, a Dirac structure) in the Bond space of effort and flow variables (i.e., the voltage and the current respectively). This Dirac structure allows, for instance, structure preserving discretization [19] or model order reduction [37] which may be needed in the analysis and supervision of grid systems [52, 36]. It may be also used in physically−based control design such as passivity−based control [33] or flatness−based approaches such as the one developed in this work.

Control approaches: Various issues, which need to be taken into account when choosing the control approach for a microgrid system, include for example different timescales or islanding and grid−connecting modes. The microgrid energy management problem is generally considered as a constrained optimization problem not straightforward to solve. A multi−level control approach is required [41] due to the existence of different timescales, the fast and the slow dynamics of the components. Generally, the hierarchical control is divided into three layers, *primary, secondary and tertiary control*, in order to be able to approach the real operation of the microgrids. The primary control (low level) includes a localized supervision of the power distribution and the voltage/current adjust-

[1]Bond Graph is a graph−oriented approach for the modular modeling of complex multiphysical systems, implemented in many existing simulation software. This graphical representation is based on the power interconnections amongst the physical elements within a dynamical system [16].

ment among the distributed energy resources (DERs) and the converters. The converters contain an internal switching activity that obeys to an external power loop based on a management strategy [48]. One such example is the maximum power point tracking [22], which includes controllers for extracting the maximum available power from solar panels or other renewable energy resources. Another approach is the master/slave control [29], where a device is selected as the master controller over one or more devices that act as slaves. Furthermore, droop control [4, 47] allows load balancing during the operation of parallel generators. The secondary control (middle level) targets the internal processes of the system under voltage and frequency disturbances. The main purpose is to reduce voltage, frequency or power deviations. These deviations can be controlled locally, but in case of a possible failure the whole system is influenced. Therefore, both centralized [40] and distributed [25] secondary controllers have been investigated and various control methods have been proposed. In [40], a phase controller is used which regulates the phase angle of the distributed generators instead of the frequency to decrease frequency and amplitude discrepancies. In [49], the authors aim to reduce the voltage deviations caused by droop control method in a distributed control framework for accuracy in current sharing. Fuzzy controllers are also investigated, for example in [50] a control structure for the aforementioned Takagi−Sugeno fuzzy systems is developed, mitigating the computational burden. [2] improves the performance of a microgrid by controlling the reactive power under disturbances caused by power outages, short circuits and the like. In [42], frequency and voltage controllers are designed, enabling the possibility to the system to achieve either frequency or voltage regulation while maintaining reactive power sharing. Predictive controllers are used such as MPC [28]. For instance [1] implements MPC in combination with a PI controller in order to decrease the discrepancies between the nominal and the actual frequency, to increase the stability of the system and to diminish the communication delays. The tertiary control (high level) deals with the power flow and optimization by taking into account different economical aspects. Here, the power flow is optimally regulated succeeding the load balancing within the transmission net-

work and providing the most economical solution. Several methods have been developed which consider the maximum generation capacity of the energy storage [30], the constraints or the uncertainties. The combined use of MPC with Mixed Integer Programming (MIP) for battery scheduling is employed in [38]. Finally, profile uncertainties are considered in an MPC framework with chance constraints and machine learning algorithms are employed in [9] for developing approximate MPC laws for household temperature control.

Amongst the methods and techniques previously described, the microgrid model is most commonly considered as a set of differential equations [35] based on constitutive equations from physics which do not explicitly represent a structure of power−preserving functions or maintain the energy conservation within the system. In addition, these systems combine fast and slow dynamics. Therefore, hierarchical control is an important and suitable tool which can manage supervision at multiple time scales. The generation of optimal profiles is strongly investigated by the researchers. Constrained optimization−based control methods are often considered such as MPC [28] MPC is a popular method to generate on−line optimal profiles for discrete−time systems. Depending on the type of MPC, the cost function penalizes the cost, the dissipation or the error among the actual and reference signal profiles. However, the microgrids are convoluted networks where numerous factors need to be examined and considered at the same time, such as power optimization, cost minimization, stability, robustness and the like. Consequently, no definitive microgrid models and control methods exist and the matters are still under investigation. In this work, a different approach, based on PH systems for modeling and differential flatness for optimal profile generation, will be presented.

Contributions: This paper is based on our previous results in [52], where the meshed DC microgrid in PH form was described and in [51] where a brief introduction of a flatness−based control approach for energy management was introduced. The contributions of this paper stem from:

- the use of the PH formalism which ensures of power−preserving intercon-

nections among all the DC microgrid's elements. Furthermore, aspects such as energy conservation, the isolation of physical quantities for further use (battery charge, voltages, etc.), dissipation conditions, etc.;

- the use of differential flatness, which is an advantageous method that allows the off-line study of physical systems in order to predict their behavior. It is considered also as a suitable tool to inverse the system dynamics: the states and inputs are given as combinations of the system's flat outputs. Furthermore, the B-spline properties ensure continuous time constraints validation (the flat output, given as a weighted sum of B-spline basis functions, is fully described by these weights);

- the multi−level control design which produces at the high and middle level optimal profiles to be followed by the lower level. For instance, power balancing requirements at the high level lead to an optimal profile for battery usage, to be tracked at the middle level; the middle level provides voltage and current references for the battery. These profiles are tracked at the low level by an explicit switching law of the DC/DC converters. In all cases we consider bottom to top information for a reliable profile generation (e.g., tracking errors are accounted for);

- the validation of the proposed hierarchical control through extensive simulations based on realistic load, renewable power and electricity price profiles. The behavior of the system is analyzed at the high, the middle and the low levels over a meshed DC grid benchmark.

Outline: This paper is organized as follows. Section 2 contains the notations. Section 3 refers to the modeling methodology and the detailed description of the ES model. Then, the flat representation for the ES is introduced with the B−spline parametrization. In section 4 the multi−layer control problem is analyzed. In section 5, the simulation results are presented and, finally, in section 6, the conclusions and the future work are highlighted.

2. Notations

ES, es	energy storage system
UG, ug	utility grid
PV, pv	solar panel system
$KiBaM$	Kinetic Battery Model
P	electrical power
Sw	switches of the Split−Pi converter
d_{1sc}	duty cycle which for Sw_4 is 1-d_{1sc} and Sw_3 is d_{1sc}
d_{2sc}	duty cycle which for Sw_1 is 1-d_{2sc} and Sw_2 is d_{2sc}
q_{1b}	available charge state of the KiBaM battery
q_{2b}	bound charge state of the KiBaM battery
r	derivative of the B-spline
p_i	i^{th} control point
$b_{i,d}$	i^{th} B-spline of order d
$\mathcal{B}(t)$	vector of the B-splines $\in R^{d\times N}$
$\mathcal{P}$	vector of control points $\in R^{3\times N}$
$\mathcal{S}_{\kappa,d-r,d}$	translation matrix from higher to lower degree basis functions
$\mathcal{M}_{d,d-r}$	matrix performing the linear combinations of the lower-degree basis functions
T	knot vector $\in R^{N+d}$
τ_κ	κ^{th} knot
κ	number of knots
e	electricity price
$Q_{\tilde{y}},\ R_{\tilde{u}}$	weight matrices
RPI	Robust Positively Invariant
$\oplus$	Minkowski sum of two sets $X_1 \in \mathbb{R}^n$ and $X_2 \in \mathbb{R}^n$ which is the result of the addition of each element in X_1 to each element in X_2
$\ominus$	Pontryagin difference of two sets $X_1 \in \mathbb{R}^n$ and $X_2 \in \mathbb{R}^n$, which is the difference between each element in X_1 and each element in X_2 resulting in another element $X_3 \in \mathbb{R}^n : X_3 + X_2 \subseteq X_1$

3. Meshed DC microgrid model description

This section follows our previous work in [51], where the meshed DC microgrid model has been primarily presented. In this work, a further analysis leads to the mathematical model of the battery attached to the Split−Pi converter. Next, the flat representation and the advantages of the associated B−spline parametrization are described, two instrumental notions for the formulation of the hierarchical control problem.

3.1. Modeling methodology

In microgrids, a decomposition into subsystems leads to a structure simplification. To achieve this decomposition and to express in detail the power interconnections among the components, a modeling methodology based on PH representation is considered. A schematic view (Bond Graph) for PH representation multiphysical systems is given in Fig.1. It is seen as the interconnection of three types of elements: i) energy sources; ii) storing elements (capacitors, inductors); iii) dissipative elements (resistors). These three components are connected through a generalized interconnection structure (Dirac structure [46] denoted by D in Fig.1) which accounts for the power continuous energy balance equations (e.g. Kirchoff's laws, ideal transformers equations in an electrical network). The general PH state−space representation of a system is [46, 10]:

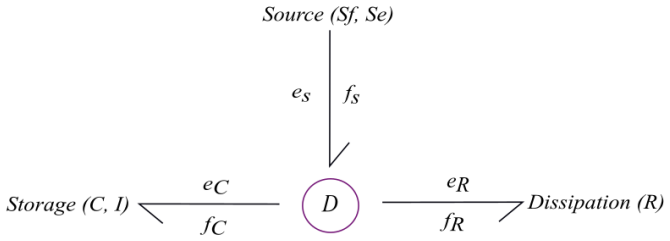

Figure 1: Schematic view for the PH formulation of a multiphysics system, where the arrows describe the power flow direction, considered as the product of associated pairs of efforts e and flows f variables. In the case of electrical circuits, e is the voltage and f is the current.

$$\begin{aligned} \dot{x}(t) &= [J(t) - R]\partial_x H(x) - Gu(t), \\ y(t) &= G^\top Q x(t) + Du(t), \end{aligned} \tag{1}$$

where $x(t) \in \mathbb{R}^n$ is the state vector of the extensive energy variables $p(t)$ and $q(t)$, which, in the case of electrical circuits, $p(t)$ is the magnetic flux of the inductors and $q(t)$ is the electrical charge of the capacitors. Furthermore, $u(t) \in \mathbb{R}^m$ is the input vector and $y(t) \in \mathbb{R}^m$ is the output vector. In the following, we explain the matrices of the PH representation: i) $J(t) \in \mathbb{R}^{n\times n}$ and $R \in \mathbb{R}^{n\times n}$ are skew$-$symmetric and symmetric positive semi definite matrices which represent the system's interconnection structure power continuity (structural balance equations which typically contain no numerical parameters) and dissipation; ii) $Q \in \mathbb{R}^{n\times n}$ is a positive definite matrix which is, in the linear case, with one$-$port[2] storage elements considered here, a diagonal matrix with the capacitance values C for the capacitors and the inductance values I for the inductors. More complex nonlinear constitutive equations may also be considered; iii) $D \in \mathbb{R}^{m\times m}$ describes the direct interconnection of the input variables and $G \in \mathbb{R}^{n\times m}$ is the control matrix.

The collocated output $y(t)$ in (1) results from the inputs selection and the input map G, in a way that the inner product among input and output vectors minus the dissipative energy gives always the external power supplied to the system [11] as you can see below:

i) The Hamiltonian H is the total energy stored in the storage elements within the system, which in the linear case is equal to the following:

$$H(x) = \frac{1}{2} x(t)^\top Q x(t); \tag{2}$$

ii) From (1) and (2) we obtain the external power supplied to the system:

$$\frac{d}{dt} H = u(t)^\top y(t) - x(t)^\top Q^\top R Q x(t) - u(t)^\top D u(t). \tag{3}$$

[2]One$-$port storage elements are the simplest components of a Bond Graph as they have only two terminals (typical examples are the capacitors and the inductors).

The power balance equation (3) is equivalent to the Tellegen's theorem, which describes the energy conservation in an electrical network. Note that the Hamiltonian H in an electrical circuit is defined as $H = \frac{1}{2}\frac{q^2}{C} + \frac{1}{2}\frac{p^2}{I}$, where q is the charge of the capacitor and p is the magnetic flux of the inductor.

3.2. DC microgrid dynamical representation

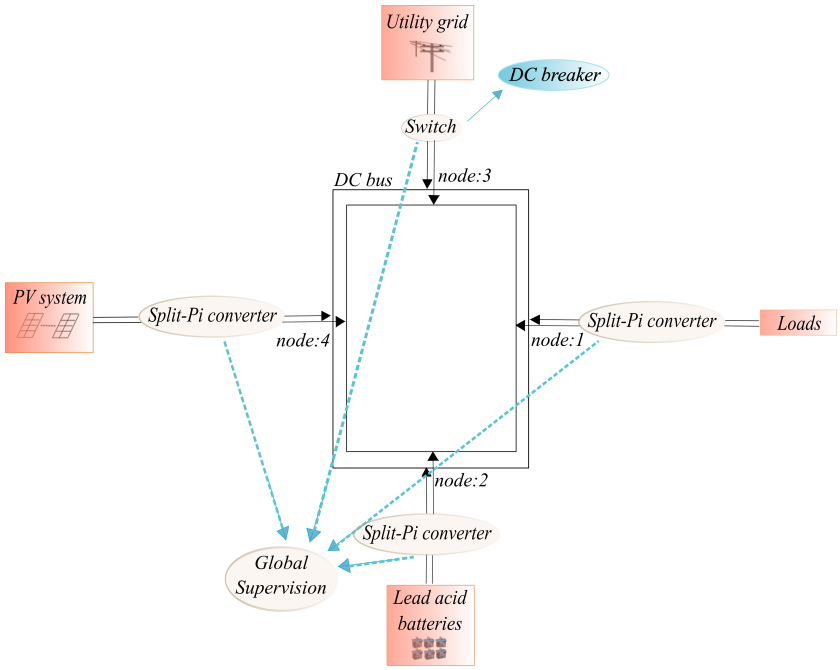

Figure 2: Meshed DC microgrid architecture.

The following work presents the meshed DC microgrid architecture (see Fig.2). A meshed topology allows the electricity transmission through a variety of sources and transmission lines. Consequently, a possible interruption of the power transmission can be avoided and the safe operation of the system can be ensured. The system is composed by a set of PVs, an ES and an ensemble of loads as in Fig.2. The global system dynamics is separated into different timescales. Primarily, the existence of the DC/DC converters useful for the voltage regulation creates a fast dynamics which needs to be stabilized around a set−point. Secondly, the slow dynamics is related to the battery and

the PV system. At the same time, we cope with variable profiles and costs and obey to a set of constraints related to the different characteristics of the system components like the battery's capacity or the permissible UG power.

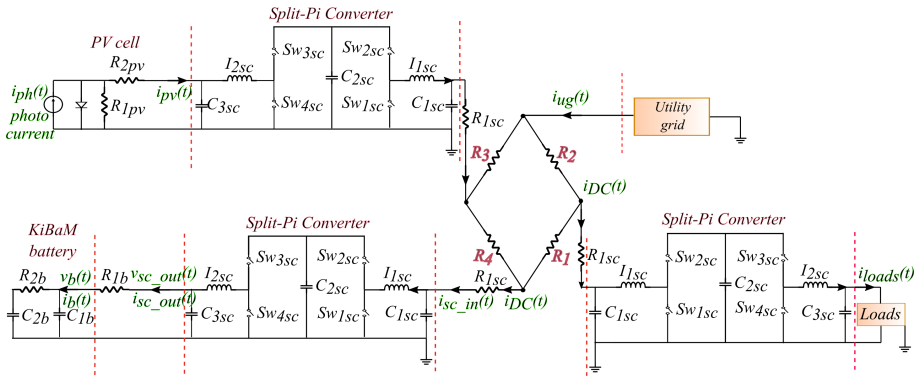

Figure 3: Corresponding electrical circuit of the DC microgrid presented in Fig.2.

Fig.3 illustrates the corresponding electrical circuit of the DC microgrid (Fig.2): its components and their links. Priority is given to the analysis of the ES since its proper operation is indispensable for the continuous power distribution and cost minimization. For the PV system, profiles are provided generated by the PV model proposed in [52], taking into account specific temperature and irradiation data. Additionally, we use specific profiles for the consumer's demand.

3.2.1. Dynamical representation of the Split−Pi/ES system

Fig. 4 illustrates the lead−acid battery/Split−Pi electrical circuit. According to the Kinetic Battery Model (KiBaM) [27], the battery consists of two capacitors (with storage capacities q_{1b} and q_{2b}) and a resistor which links them. In the following, the associated PH model is presented:

$$\begin{cases} \dot{x}_{es}(t) &= [J_{es}(d(t)) - R_{es}]Q_{es}x_{es}(t) + G_{es}u_{es}(t), \\ y_{es}(t) &= G_{es}^{\top}Q_{es}x_{es}(t) + D_{es}u_{es}(t), \end{cases} \tag{4}$$

where $x_{es}(t) = \begin{bmatrix} p_{1sc}(t) & p_{2sc}(t) & q_{1sc}(t) & q_{2sc}(t) & q_{3sc}(t) & q_{1b}(t) & q_{2b}(t) \end{bmatrix}^\top \in R^{7\times 1}$, $u_{es}(t) = \begin{bmatrix} -v_{DC}(t) & -i_{R_{1b}}(t) \end{bmatrix}^\top \in R^{2\times 1}$, $y_{es}(t) = \begin{bmatrix} i_{DC}(t) & v_{R_{1b}}(t) \end{bmatrix}^\top \in R^{1\times 2}$, where $i_{DC}(t)$ is the current during charging mode. Additionally, the

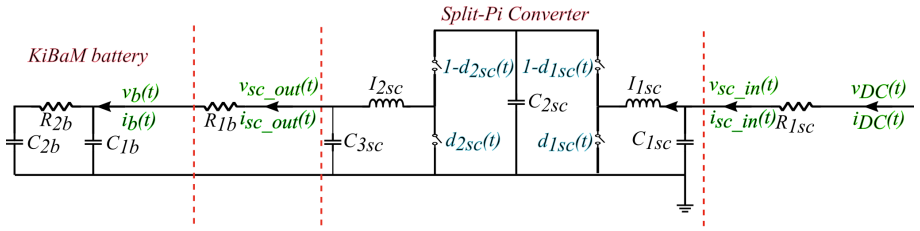

Figure 4: Detailed electrical network of the ES system during charging mode. The notations of the switches (Sw_{1sc}, Sw_{2sc}, Sw_{3sc}, Sw_{4sc}) have been replaced by the corresponding duty cycles d_{1sc} and d_{2sc}.

diagonal matrix Q_{es} is equal to diag($1/I_{1sc}$, $1/I_{2sc}$, $1/C_{1sc}$, $1/C_{2sc}$, $1/C_{3sc}$, $1/C_{1b}$, $1/C_{2b}$) $\in R^{7\times 7}$. The skew-symmetric matrix $J_{es}(t) \in R^{7\times 7}$, the dissipation matrix $R_{es} \in R^{7\times 7}$, the $G_{es}^\top \in R^{2\times 7}$ and $D_{es} \in R^{2\times 2}$ are equal to:

$$J_{es}(t) = \begin{bmatrix} 0 & 0 & 1 & -(1-d_{1sc}(t)) & 0 & 0 & 0 \\ 0 & 0 & 0 & (1-d_{2sc}(t)) & -1 & 0 & 0 \\ -1 & 0 & 0 & 0 & 0 & 0 & 0 \\ 1-d_{1sc}(t) & -(1-d_{2sc}(t)) & 0 & 0 & 0 & 0 & 0 \\ 0 & 1 & 0 & 0 & 0 & 0 & 0 \\ 0 & 0 & 0 & 0 & 0 & 0 & 0 \\ 0 & 0 & 0 & 0 & 0 & 0 & 0 \end{bmatrix}, \quad (5)$$

$$R_{es} = \begin{bmatrix} 0 & 0 & 0 & 0 & 0 & 0 & 0 \\ 0 & 0 & 0 & 0 & 0 & 0 & 0 \\ 0 & 0 & \frac{1}{R_{1_{sc}}} & 0 & 0 & 0 & 0 \\ 0 & 0 & 0 & 0 & 0 & 0 & 0 \\ 0 & 0 & 0 & 0 & 0 & 0 & 0 \\ 0 & 0 & 0 & 0 & 0 & \frac{1}{R_{1b}} + \frac{1}{R_{2b}} & -\frac{1}{R_{2b}} \\ 0 & 0 & 0 & 0 & 0 & -\frac{1}{R_{2b}} & \frac{1}{R_{2b}} \end{bmatrix}, \quad (6)$$

$$G_{es}^{\top} = \begin{bmatrix} 0 & 0 & \dfrac{-1}{R_{1_{sc}}} & 0 & 0 & 0 & 0 \\ 0 & 0 & 0 & 0 & 1 & -1 & 0 \end{bmatrix}, D_{es} = \begin{bmatrix} \dfrac{1}{R_{1sc}} & 0 \\ 0 & 0 \end{bmatrix} \tag{7}$$

where $d_{1sc}(t)$, $d_{2sc}(t)$ are the control variables of our system. All the unknown variables and parameters of the battery model can be found in the literature and depend on the type of the lead−acid battery. The Split−Pi converter switches control the charging and the discharging of the battery.

3.3. Dynamical representation of the central transmission network

The transmission network model (4−line transmission network, see Fig.3) is also represented by using the Bond Graph method [52]. Its dynamical representation is presented below:

$$\begin{aligned} &P_{ug}(t)+P_{pv}(t) - P_{es}(t) - P_{loads}(t) - P_{R1}(t)- \\ &-P_{R2}(t) - P_{R3}(t) - P_{R4}(t) = 0, \end{aligned} \tag{8}$$

where $P_{ug}(t) = i_{ug}(t) \cdot v_{ug}(t)$ and $P_{es}(t) = i_b(t) \cdot v_b(t)$. At first, because of the complexity of the equations, the power losses within the transmission central network are not considered in this work and are equal to 0:

$$P_{R1}(t) = P_{R2}(t) = P_{R3}(t) = P_{R4}(t) = 0. \tag{9}$$

Combining (8) and (9) the power conservation equation becomes:

$$P_{ug}(t) + P_{pv}(t) - P_{es}(t) - P_{loads}(t) = 0. \tag{10}$$

3.3.1. Flat representation of the ES connected to the Split−Pi converter

Hereinafter, the ES state−space representation model (4, 5, 6, 7, 10) will be rewritten in function of the flat outputs of the system using the differential flatness notion. Differential flatness allows to describe the system's states and inputs as algebraic combinations of the flat outputs and a finite number of their derivatives. In turn, the flat output is an algebraic combination of states and input derivatives [12]. A nonlinear system [12]:

$$\dot{x} = f(x, u), \tag{11}$$

with $x \in R^n$ the state vector and $u \in R^m$ the input vector , for which $f(0,0) = 0$ and $rank\dfrac{\partial f}{\partial u} = m$ are verified, can be characterized as differentially flat, if there exists a flat output vector $z = [z_1\ z_2\ ...\ z_m]^\top$ which satisfies the following conditions: i) the flat output z is presented in function of the states and the inputs of the system and their derivatives, $z = \Phi(x, u, \dot{u}, \ddot{u}, ...)$; ii) the states and the inputs of the system (4, 5, 6, 7) are described in terms of the flat outputs and a finite number of their derivatives, $x = \Phi_x(z, \dot{z}, \ddot{z}, ...)$ and $u = \Phi_u(z, \dot{z}, \ddot{z}, ...)$; iii) the flat outputs z and their derivatives are differentially independent.

Flatness and controllability are two associated properties. In [12] it is demonstrated that a nonlinear system is flat if and only if it is controllable. Finding the flat outputs set for nonlinear systems is convoluted. The literature provides useful approaches, such as the algorithm proposed by [13], which is a methodical computation of flat outputs for nonlinear control systems. The algorithm uses symbolic linearization of the system to generate flat outputs. A subsequent calculation of matrices, nullspaces and inverses leads to a set of the corresponding flat outputs through integration. The algorithm simultaneously verifies if the system is not controllable and, consequently, not flat [21].

The dynamical PH model presented in (4), (5), (6) and (7) has two inputs ($v_{DC}(t)$, $i_{R_{1b}}(t)$). The duty cycles ($d_{1sc}(t)$, $d_{2sc}(t)$), as control variables, are considered also as inputs to the system. According to [12], the number of flat outputs is equal to the number of inputs, which means that four flat outputs need to be found. Therefore, the four flat outputs provided by the algorithm are the following:

$$z_1(t) = \frac{1}{I_{1sc}}\frac{p_{1sc}(t)^2}{2} + \frac{1}{I_{2sc}}\frac{p_{2sc}(t)^2}{2} + \frac{1}{C_{2sc}}\frac{q_{2sc}(t)^2}{2}, \tag{12a}$$

$$z_2(t) = q_{3sc}(t) + q_{1b}(t), \tag{12b}$$

$$z_3(t) = q_{2b}(t), \tag{12c}$$

$$z_4(t) = q_{2sc}(t). \tag{12d}$$

The flat outputs are in function of the states $p_{1sc}(t)$, $p_{2sc}(t)$, $q_{3sc}(t)$, $q_{1b}(t)$, $q_{2b}(t)$. Substituting (12a)$-$(12d) into the PH model (4$-$7), the remaining states

and inputs are written in function of the flat outputs. Appendix A presents the detailed flat representation of the system. Below, the general flat representation of the system is written where the states and the inputs are described in function of the flat outputs (12a−12d) and their derivatives[3]:

$$p_{1sc}(t) = \Phi_1(z_1, \dot{z}_2, z_3, \dot{z}_3, z_4), \tag{13a}$$

$$p_{2sc}(t) = \Phi_2(\dot{z}_2, z_3, \dot{z}_3), \tag{13b}$$

$$q_{1sc}(t) = \Phi_3(z_1, \dot{z}_1, z_2, \dot{z}_2, \ddot{z}_2, z_3, \dot{z}_3, \ddot{z}_3, z_4, \dot{z}_4), \tag{13c}$$

$$q_{2sc}(t) = \Phi_4(z_4), \tag{13d}$$

$$q_{3sc}(t) = \Phi_5(z_2, z_3, \dot{z}_3), \tag{13e}$$

$$q_{1b}(t) = \Phi_6(z_3, \dot{z}_3), \tag{13f}$$

$$q_{2b}(t) = \Phi_7(z_3), \tag{13g}$$

$$d_{1sc}(t) = \Phi_8(z_1, z_2, \dot{z}_2, \ddot{z}_2, z_3, \dot{z}_3, \ddot{z}_3, z_4), \tag{13h}$$

$$d_{2sc}(t) = \Phi_9(z_2, \ddot{z}_2, z_3, \dot{z}_3, \ddot{z}_3, z_4), \tag{13i}$$

$$v_{DC}(t) = \Phi_{10}(z_1, \dot{z}_1, \ddot{z}_1, z_2, \dot{z}_2, \ddot{z}_2, \dddot{z}_2, z_3, \dot{z}_3, \ddot{z}_3, \dddot{z}_3, z_4, \dot{z}_4, \ddot{z}_4), \tag{13j}$$

$$i_{R_{1b}}(t) = \Phi_{11}(\dot{z}_3, \ddot{z}_3). \tag{13k}$$

Next, the B−splines curves are employed, an appropriate tool for flat output parametrization due to its properties of convexity, smoothness and differentiability used for continuous−time constraints validation. The B−splines degree depends on the highest order derivative where the continuity needs to be ensured. Hence, in the following the flat output $z(t)$ is projected over N B−splines of order d [44]:

$$z(t) = \sum_{i=1}^{N} p_i \cdot b_{i,d}(t) = \mathcal{P}\mathcal{B}_d(t), \tag{14}$$

where $p_i \in \mathbb{R}^3$ is gathered into the matrix $\mathcal{P} \in \mathbb{R}^{3\times N}$ of N control points, $\mathcal{P} = \begin{bmatrix} p_1 & p_2 & ... & p_N \end{bmatrix}$. In (14) $\mathcal{B}_d(t) = \begin{bmatrix} b_{1,d}(t) & b_{2,d}(t) & ... & b_{N,d}(t) \end{bmatrix}^\top$ is the

[3]Wherever it is straightforward implied by the text, we discard the time dependence.

B−spline vector. Furthermore, the B−splines are defined over a knot−vector $T = \{\tau_0 \leq \tau_1 \leq ... \leq \tau_m\} \in \mathbb{R}^{N+d}$ which is a set of non−decreasing time instants with $m = N + d + 1$. More details on the theory and the properties of B−splines, employed in the following section, can be found in [43].

4. Hierarchical constrained optimization−based control

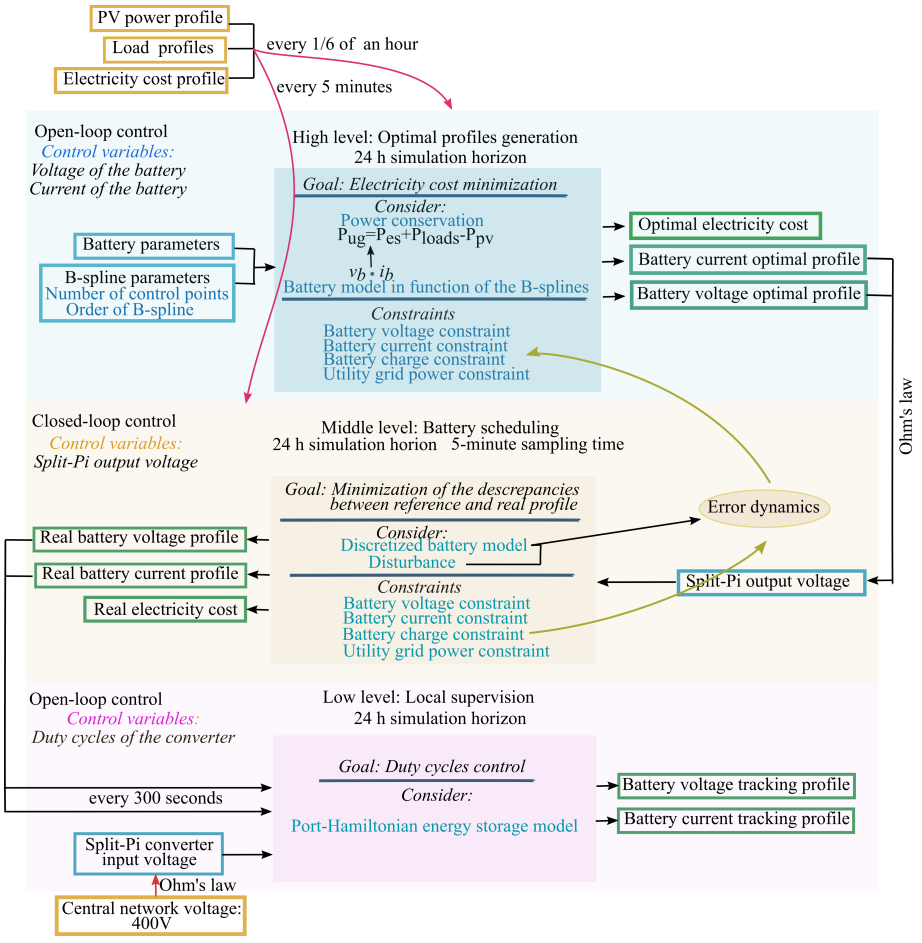

Figure 5: Flowchart of the hierarchical control for the DC microgrid.

This section analyzes the hierarchical control problem. The main goal is to reduce the electricity cost by minimizing the energy consumption of the UG,

hence taking advantage of the PV power production and the ES system capacity. The control variables of the ES system (4, 5, 6, 7) are the duty cycles of the Split−Pi converter (5), $d_{1sc}(t)$, $d_{2sc}(t)$, and the power generated from the UG, $P_{ug}(t)$. Considering all the elements introduced in section 3, the hierarchical control approach is presented in Fig. 5: i) *high level* (power flow optimization): optimal profiles for the battery current i_b and voltage v_b are generated by an optimization problem with continuous−time constraint validation ensured by the B−splines properties; ii) *middle level* (battery scheduling): a tube−MPC tracking mechanism [20] is employed which provides an efficient battery scheduling under current and voltage additive noises; iii) *low level* (switching activity in the converter): an explicit control law for the duty cycles of the converter is provided for tracking the a priori given battery current and voltage profiles.

4.1. High level control

Hereinafter, the high level considers the minimization of the power generated by the UG (with $P_{ug}(t) = -P_{pv}(t)+P_{es}(t)+P_{loads}(t)$ as in (10)) while satisfying the ES system dynamics (4, 5, 6, 7) and the constraints:

$$\min_{i_b(t),v_b(t)} \int_{t_0}^{t_f} e(t)(\underbrace{P_{es}(t)}_{i_b(t)v_b(t)} + P_{loads}(t) - P_{pv}(t))dt, \tag{15a}$$

$$subject\ \ to:\ the\ system\ dynamics\ (13a) - (13k), \tag{15b}$$

$$v_b^{min,h} \leq v_b(t) \leq v_b^{max,h}, \tag{15c}$$

$$i_b^{min,h} \leq i_b(t) \leq i_b^{max,h}, \tag{15d}$$

$$q_{2b}^{min,h} \leq q_{2b}(t) \leq q_{2b}^{max,h}, \tag{15e}$$

$$P_{ug}^{min,h} - P_{loads}(t) + P_{pv}(t) \leq P_{es}(t) \leq P_{ug}^{max,h} + P_{loads}(t) - P_{pv}(t), \tag{15f}$$

with the control variables being the battery's voltage, v_b, and the battery's current, i_b. Replacing in (15a)−(15f) the ES power in terms of the control variables, i_b, v_b, we obtain a nonlinear optimization problem. Furthermore, considering $q_{1b}(t)$ and $i_{R_{1b}}(t)$ from (4) (which verify $i_b(t) = i_{R_{1b}}(t)$ and $v_b(t) = \frac{q_{1b}(t)}{C_{1b}}$) in function of the flat outputs as in (13f) and (13k), the voltage and

current profile references are expressed as:

$$v_b(t) = \frac{1}{C_{2b}} z_3(t) + R_{2b}\dot{z}_3(t), \tag{16a}$$

$$i_b(t) = (1 + \frac{C_{1b}}{C_{2b}})\dot{z}_3(t) + C_{1b}R_{2b}\ddot{z}_3(t). \tag{16b}$$

Next in (16a) and (16b), we continue with the B−spline parametrization of $z_3(t)$:

$$v_b(t) = \sum_{i=1}^{N} \left(\frac{1}{C_{2b}}\mathcal{P} + R_{2b}\mathcal{P} \right) \mathcal{B}_d^{(r)}(t), \tag{17a}$$

$$i_b(t) = \sum_{i=1}^{N} \left[\left(1 + \frac{C_{1b}}{C_{2b}} \right) \mathcal{P} + C_{1b}R_{2b}\mathcal{P} \right] \mathcal{B}_d^{(r)}(t). \tag{17b}$$

In (17a) and (17b) the differentiation property of the B−splines is employed. The $r-$order derivatives of $d-$order B−splines can be expressed as $d-r$ order B−splines which, in turn, can be expressed as $d-$order B−splines over each knot sub−interval:

$$\mathcal{B}_d^{(r)}(t) = M_{d,d-r}\mathcal{B}_{d-r}(t) = M_{d,d-r}S_{\kappa,d-r,d}\mathcal{B}_d(t), \ \ \forall t \in [\tau_\kappa, \tau_{\kappa+1}). \tag{18}$$

From (14), (16b), (16a) and (18), the battery's output current and voltage are derived in function of the B−splines:

$$v_b(t) = \sum_{i=1}^{N} \left[\frac{1}{C_{2b}} p_i + R_{2b} \left(\mathcal{P}M_{d,d-1}S_{\kappa,d-1,d} \right)_i \right] \mathcal{B}_{i,d}(t), \tag{19a}$$

$$i_b(t) = \sum_{i=1}^{N} \left[\left(1 + \frac{C_{1b}}{C_{2b}} \right) \left(\mathcal{P}M_{d,d-1}S_{\kappa,d-1,d} \right)_i + C_{1b}R_{2b} \cdot \left(\mathcal{P}M_{d,d-2}S_{\kappa,d-2,d} \right)_i \right] \cdot$$

$$\cdot \mathcal{B}_{i,d}(t), \ \ \forall t \in [\tau_\kappa, \tau_{\kappa+1}) \, . \tag{19b}$$

The representation obtained in (19a) and (19b) is introduced in the cost function and the constraints of the optimization problem (15a)−(15f). Hence, it is rewritten in function of the B−splines and a finite number of control variables represented by the control points. For the detailed calculation, see Appendix B. The reference profiles obtained at the high level for the battery current and voltage will be denoted in the middle level as i_b^{ref} and v_b^{ref}, respectively.

4.2. Middle level control

In this section, a tube−MPC controller is developed to track the output voltage reference profile, $v_{sc\_out}^{ref}$, of the Split−Pi converter under bounded noise. Note that the output voltage reference of the converter can be written in function of the battery current and voltage reference profiles obtained at the high level from (15a)−(15f) following:

$$v_{sc\_out}^{ref}(t) = v_b^{ref}(t) + i_b^{ref}(t)R_{1b}. \tag{20}$$

Using the Euler explicit method, the battery dynamics is discretized with the charges of the battery, q_{1b} and q_{2b}, as state variables, the output voltage from the Split−Pi converter, v_{sc_out}, as input variable and the current and voltage of the battery, v_b and i_b, as output variables, considered as $\tilde{x}(k) = \begin{bmatrix}\tilde{q}_{1b}(k) & \tilde{q}_{2b}(k)\end{bmatrix}^\top$, $\tilde{u}(k) = \tilde{v}_{sc\_out}(k)$ and $\tilde{y}(k) = \begin{bmatrix}\tilde{i}_b(k) & \tilde{v}_b(k)\end{bmatrix}^\top$, where $\tilde{i}_b(k) = \tilde{i}_{sc}(k)$ and $\tilde{v}_b(k) = \dfrac{\tilde{q}_{1b}(k)}{C_{1b}}$ (see the ES circuit in Fig.4). Therefore, the obtained discretized system is presented as follows:

$$\begin{cases} \tilde{x}(k+1) &= A\tilde{x}(k) + B\tilde{u}(k), \\ \tilde{y}(k) &= C\tilde{x}(k) + D\tilde{u}(k), \end{cases} \tag{21}$$

with $A = \begin{bmatrix} 1 - \dfrac{T_s}{C_{1b}}\left(\dfrac{1}{R_{1b}} + \dfrac{1}{R_{2b}}\right) & \dfrac{T_s}{C_{2b}R_{2b}} \\ \dfrac{T_s}{C_{1b}R_{2b}} & 1 - \dfrac{T_s}{C_{2b}R_{2b}} \end{bmatrix}$, $B = \begin{bmatrix} \dfrac{T_s}{R_{1b}} \end{bmatrix}$,
$C = \begin{bmatrix} -\dfrac{1}{C_{1b}R_{1b}} & 0 \\ \dfrac{1}{C_{1b}} & 0 \end{bmatrix}$, $D = \begin{bmatrix} \dfrac{1}{R_{1b}} \\ 0 \end{bmatrix}$ and T_s the sampling time.

Next, a tracking MPC formulation is proposed in which the cost penalizes the tracking error (the difference between actual and reference output profiles) over a finite prediction horizon N_p:

$$\min_{\tilde{u}(k)} \sum_{i=k}^{k+N_p-1} (\tilde{y}(i) - \tilde{y}^{ref}(i))^\top Q_{\tilde{y}} (\tilde{y}(i) - \tilde{y}^{ref}(i)) + \\ + (\tilde{u}(i) - \tilde{u}^{ref}(i))^\top R_{\tilde{u}} \left(\tilde{u}(i) - \tilde{u}^{ref}(i)\right) \tag{22a}$$

$$subject\ \ to:\ the\ system\ dynamics\ (21), \tag{22b}$$

$$\tilde{v}_b^{min,m} \leq \tilde{v}_b(k) \leq \tilde{v}_b^{max,m}, \tag{22c}$$

$$\tilde{i}_b^{min,m} \leq \tilde{i}_b(k) \leq \tilde{i}_b^{max,m}, \tag{22d}$$

$$\tilde{q}_{2b}^{min,m} \leq \tilde{q}_{2b}(k) \leq \tilde{q}_{2b}^{max,m}, \tag{22e}$$

$$\tilde{P}_{ug}^{min,m} \leq \tilde{P}_{ug}(k) \leq \tilde{P}_{ug}^{max,m}, \tag{22f}$$

with $\tilde{y}^{ref}(k) = \begin{bmatrix} \tilde{i}_b^{ref}(k) & \tilde{v}_b^{ref}(k) \end{bmatrix}^\top$, the current and voltage references of the battery, and $\tilde{u}^{ref}(k) = \tilde{v}_{sc\_out}^{ref}(k)$, the output voltage reference of the Split−Pi converter, taken at T_s sampling time. The control variable of the tracking problem is the output voltage of the Split-Pi converter, v_{sc_out}. The last constraint $P_{ug}(t)$ is rewritten below:

$$\tilde{P}_{ug}^{min,m} - \tilde{P}_{loads}(k) + \tilde{P}_{pv}(k) \leq \tilde{P}_{es}(k) \leq \tilde{P}_{ug}^{max,m} - \tilde{P}_{loads}(k) + \tilde{P}_{pv}(k), \tag{23}$$

where $\tilde{P}_{es}(k) = \tilde{i}_b(k)\tilde{v}_b(k)$ as aforementioned. The aforementioned objective function is in quadratic form with nonlinear constraints and a variable electricity cost. Additionally, the profiles of the PV, the loads demand and the electricity price are taken into account. Furthermore, the problem is formulated to track the profiles under perturbations.

At the high level, a desired profile is generated for the voltage, v_b, and the current, i_b, of the battery. The dynamics considered at the middle level has to follow these profiles (replaced by the output voltage of the Split−Pi converter v_{sc_out}) as best as possible. The considered approach is the so−called *tube−MPC* [20] where an MPC law provides the nominal input (based on the nominal, noise−free dynamics) and the actual input adds to the nominal value a corrective term which counteracts the noise.

The tracking error, under certain assumptions, can be bounded by an RPI set. Since the profile to be tracked is generated at the high level we can tighten the constraints considered in its design so as to guarantee reliability under noises (with the tightening factor being defined by the aforementioned RPI set). The pair of nominal input and nominal state $(\tilde{u}(k), \tilde{x}(k)$ are considered generated

by the repeated application of a MPC law over the nominal dynamics of the battery (24b). Furthermore, the real dynamics (24a) is affected by the bounded noise $\tilde{w}(k)$:

$$\tilde{x}_w(k+1) = A\tilde{x}_w(k) + B\tilde{u}_w(k) + \tilde{w}(k), \tag{24a}$$

$$\tilde{x}(k+1) = A\tilde{x}(k) + B\tilde{u}(k), \tag{24b}$$

where $\tilde{w}(k)$ is the perturbation, $\tilde{x}(k)$ is the nominal state and $\tilde{x}_w(k)$ is the real, noise−affected, state. Linking the nominal and actual inputs through the relation $\tilde{u}_w(k) = \tilde{u}(k) + K(\tilde{x}(k)\text{-}\tilde{x}_w(k))$ allows us to write the tracking error dynamics as:

$$s(k+1) = (A + BK)s(k) + \tilde{w}(k). \tag{25}$$

For any controllable pair $(A,\ B)$ in (25), there exists a static feedback K such that $(A + BK)$ is stable which means that there exists an RPI set $\mathcal{S}$ for which $s(k) \in S\ \forall\ k \geq k_0$ holds. Such a set can be computed with the ultimate bounds method [18] or iterative procedures [32].

Having $s(k) \in S$ is equivalent with $\tilde{x}_w(k) \in \{\tilde{x}(k) \oplus S\}$ (note that $\oplus$ is the Minkowski sum). In other words, the nominal $\tilde{x}(k)$ has to be chosen more conservatively than $\tilde{x}_w(k)$. Thus, to ensure that $\tilde{x}_w(k) \in \tilde{X} = \{x^{min,m} \leq x \leq x^{max,m}\}$, $\tilde{x}(k)$ is limited as follows:

$$\tilde{x}(k) \in \tilde{X} \ominus S \tag{26}$$

Note that the restriction on $\tilde{x}(k)$ translates to a similar restriction on $\tilde{y}(k)$:

$$\tilde{y}(k) \in \tilde{Y} \ominus \mathcal{C}S, \tag{27}$$

where $\tilde{Y}$ is a shorthand notation for constraints (22c), (22d) and (22f). The $\ominus$ symbol refers to the Pontryagin difference. The same tightening term $\mathcal{C}S$ is considered in the profile generation implemented at the high level as in (19a)−(19b).

4.3. Low level control

The low level control focuses on the fast dynamics of the system caused by the switching activity within the Split−Pi converter. The tracking profiles

obtained in the middle level are taken into account as references for the duty cycles supervision. In order to proceed to the analysis of the Split−Pi converter system, we follow the patent of United States Patent and Trademark Office No: US 6914420 B2 published on July 2005 [7]. The patent provides the relations among the input/output voltage (v_{sc_in}, v_{sc_out}) and the duty cycles (d_{1sc}, d_{2sc}) of the converter. Notice that the output voltage v_{sc_out} is always between 12-13 V, according to the battery's parameters considered later in the simulations, and the input voltage v_{sc_in} is always approximately equal to 400 V. Therefore, the Split−Pi converter always operates in down−conversion during battery's charging (positive direction) and up−conversion during battery's discharging (negative direction). Consequently, only the duty cycle d_{2sc} can take values from 0 to 1 (on/off switching between Sw_3 and Sw_4) and the duty cycle d_{1sc} is always equal to 0 (Sw_2 is always off and Sw_1 is always on). Therefore, the control variable is d_{2sc} and obeys to the relations below:

$$\frac{v_{sc\_out}(t)}{v_{sc\_in}(t)} = 1 - d_{2sc}(t) \tag{28}$$

where, from Ohm's law,

$$v_{sc\_in}(t) = v_{DC}(t) - i_{DC}(t)R_{1sc}, \tag{29}$$

$$v_{sc\_out}(t) = v_b(t) + i_b(t)R_{1b}. \tag{30}$$

Moreover, since there is no dissipation within the converter, at the equilibrium point, where $\dot{p}_{isc} = 0$ and $\dot{q}_{isc} = 0$, the total energy contained in the capacitors and inductors is preserved. Therefore, the relation below is deduced:

$$u_{sc\_in}(t)i_{sc\_in}(t) = u_{sc\_out}(t)i_{sc\_out}(t), \tag{31}$$

$$i_{DC}(t)v_{sc\_in}(t) = i_b(t)v_{sc\_out}(t). \tag{32}$$

Substituting equations (29), (30), (32) in (28) concludes in the relation below:

$$d_{2sc}(t) = 1 - \frac{v_{DC}(t) - \sqrt{v_{DC}^2(t) - 4(v_{sc\_out}(t) - v_b(t))(v_{sc\_out})}}{2(v_{sc\_out}(t) - v_b(t))}. \tag{33}$$

The duty cycle d_{2sc} is the control variable of the low level. The last equation (33) can be valid only if $v_{sc\_out}(t) \neq v_b(t)$ as in (20) and (16a).

5. Simulation results

In this section, we present the simulation results of the three levels of the hierarchical control design. In tables 1 and 2, the parameters of the DC microgrid and the simulation settings are indicated for the the high and the middle levels.

Table 1: Model parameters for the simulations

Variable	Values	Units
R_{1sc}, R_{1b}, R_{2b}	0.1, 0.025, 0.088	$[\Omega]$
I_{1sc}, I_{2sc}	0.25, 0.25	$[H]$
C_{1sc}, C_{2sc}, C_{3sc}	0.0008, 0.0008, 0.0008	$[F]$
C_{1b}, C_{2b}	86400, 21600	$[F]$

Table 2: System settings for the simulations

	Variable	Values	Units
High level	N as in (19a),(19b)	18	
	d as in (19a),(19b)	4	
Constraints	$v_b^{min,h} \leq v_b(t) \leq v_b^{max,h}$	$12.1 \leq v_b(t) \leq 12.9$	$[V]$
	$i_b^{min,h} \leq i_b \leq i_b^{max,h}$	$-9 \leq i_b(t) \leq 9$	$[A]$
	$q_{1b}^{min,m} \leq q_{1b}(t) \leq q_{1b}^{max,m}$	$290 \leq q_{1b}(t) \leq 307$	$[Ah]$
	$q_{2b}^{min,h} \leq q_{2b}(t) \leq q_{2b}^{max,h}$	$72.5 \leq q_{2b}(t) \leq 77.5$	$[Ah]$
	$P_{ug}^{min,h} \leq P_{ug}(t) \leq P_{ug}^{max,h}$	$-2100 \leq P_{ug}(t) \leq 4200$	$[W]$
Middle level	N_p as in (22a)	10	$[h]$
	T_s as in (21)	300	$[s]$
	Q_y as in (22a)	$diag(1,1)$	
	R_u as in (22a)	800	
Constraints	$v_b^{min,m} \leq \tilde{v}_b(k) \leq v_b^{max,m}$	$12 \leq \tilde{v}_b(k) \leq 13$	$[V]$
	$i_b^{min,m} \leq \tilde{i}_b(k) \leq i_b^{max,m}$	$-10 \leq \tilde{i}_b(k) \leq 10$	$[A]$
	$q_{1b}^{min,m} \leq \tilde{q}_{1b}(k) \leq q_{1b}^{max,m}$	$288 \leq \tilde{q}_{1b}(k) \leq 308$	$[Ah]$
	$q_{2b}^{min,m} \leq \tilde{q}_{2b}(k) \leq q_{2b}^{max,m}$	$72 \leq \tilde{q}_{2b}(k) \leq 78$	$[Ah]$
	$P_{ug}^{min,m} \leq \tilde{P}_{ug}(k) \leq P_{ug}^{max,m}$	$-2100 \leq \tilde{P}_{ug}(k) \leq 4200$	$[W]$

For the simulations we use a set of DS−100 PV modules (180 W peak PV generation) with external temperature and irradiation profiles gathered for a

whole summer day [5]. Through the model developed in [52] implemented in MATLAB/Simulink, we obtain the power profiles for the PV system. For the ES system in (4), a collection of AGM 12−165 lead acid batteries (165 Ah battery capacity) is considered. Additionally, for the load profiles, two types of loads are provided, one for commercial use (4308 W peak demand) [31], where the demand is higher during the day, and one for domestic use (3901 W peak demand) [8], where the demand increases after 4 p.m.. Concerning the electricity price, the cost varies between 0.147 $[euros/kWh]$ from 4 p.m. to 10 p.m. and 0.116 $[euros/kWh]$ for the rest of the day. The DC microgrid is connected to the UG (4200 W maximum UG generation) through a DC breaker, as shown in Fig.2. MATLAB 2015a version is used for the simulations. Furthermore, the YALMIP [23] tool is applied for both high and middle level optimization. This tool allows the use of the IPOPT solver [3], capable to handle nonlinear formulations. For the low level, we design and implement the ES system in MATLAB/Simulink in order to validate the proper operation of the switching activity within the Split−Pi converter.

We a priori choose the constraints for the current and the voltage of the battery at the high level according to the RPI set computation (24b). At this point, disturbances are added to the system's input variable, which is the output voltage of the Split−Pi converter ($\tilde{v}_{sc\_out}$) of the middle level, equal to 5% of the difference between the minimum and the maximum value of $\tilde{v}^{ref}_{sc\_out}$ in (22a). In Table 2, the constraints chosen for the high level are restricted with respect to the constraints chosen for the middle level.

Fig.6 and Fig.7 present the RPI set $\mathcal{S}$ and the nominal and noise−affected variables. The sets at several time instants highlight that the profiles are robust under bounded noise (i.e., the real trajectory lies in a tube centered around the nominal trajectory). Below the corresponding RPI set is written:

$$\mathcal{S} \triangleq \left\{ \begin{bmatrix} \text{-0.38 } [Ah] \\ \text{-0.11 } [Ah] \end{bmatrix} \leqslant \begin{bmatrix} \tilde{q}_{w_{1b}} \text{-} \tilde{q}_{1b} \\ \tilde{q}_{w_{2b}} \text{-} \tilde{q}_{2b} \end{bmatrix} \leqslant \begin{bmatrix} 0.38 \ [Ah] \\ 0.11 \ [Ah] \end{bmatrix} \right\} \tag{34}$$

and the associated static feedback $K = \begin{bmatrix} 0.685 \cdot 10^{-4} & 0.139 \cdot 10^{-4} \end{bmatrix}$ as in (25).

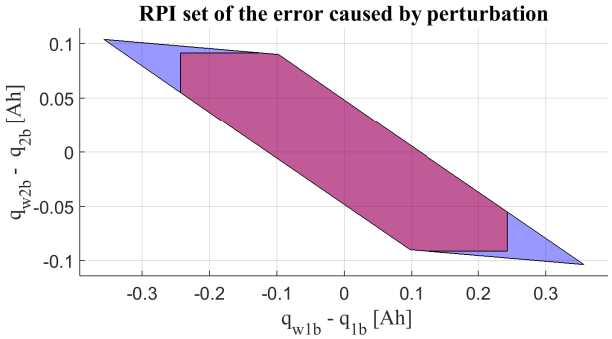

Figure 6: RPI set S of the model states.

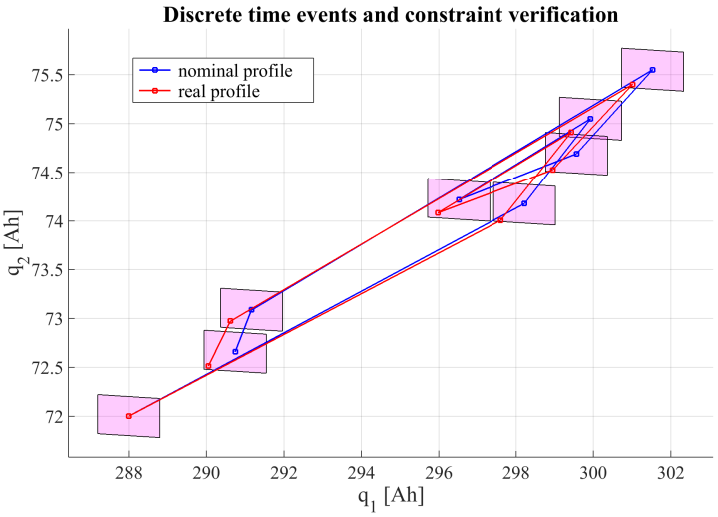

Figure 7: Ultimate bounds for discrete time events of the model states, $\tilde{q}_{1b}$ and $\tilde{q}_{2b}$ following the commercial use load profile.

Hence, it can be verified that the states, $\tilde{q}_{1b}$ and $\tilde{q}_{2b}$ (Fig. 8), lie in the RPI set.

High level: First, the simulation results of the high level in Fig.9 are presented for both commercial (Fig.9a) and domestic load (Fig.9b) profiles generated through a B−spline parametrization, as in section 4.1, with $N = 18$ control points. The simulation is based on a constrained open−loop dynamics implementation in continuous−time over a horizon of 24 hours. The profiles of the PV and the loads are imported at the beginning with a sampling time equal to 600 s. Note that the power positive sign indicates the power supplied to the microgrid. Fig.9a and Fig. 9b depict the power profiles generated by the

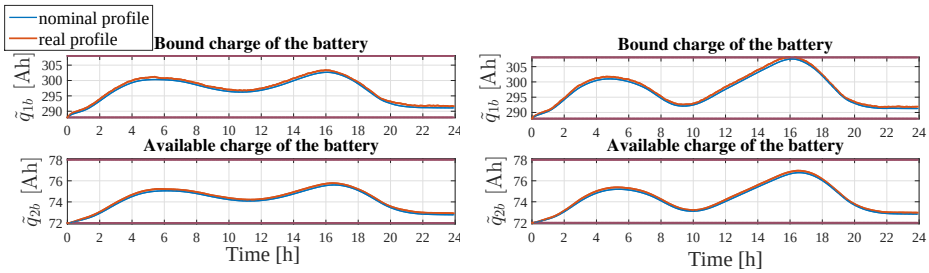

Figure 8: (a) ES system states $\tilde{q}_{1b}$ and $\tilde{q}_{2b}$ with (real profile) and without (nominal profile) perturbation (commercial use load profile). (b) ES system states $\tilde{q}_{1b}$ and $\tilde{q}_{2b}$ with and without perturbation (domestic use load profile). The red lines represent the corresponding constraints.

ES and the UG within 24 hours (power balancing), taking into account the PV and the consumers' demand profiles for commercial and domestic use. For the commercial load profile, the demand is high during the day from 6 a.m. to 4 p.m.. On the other hand, the domestic load demand increases during the afternoon after 4 p.m.. In Table 3 percentages of the power produced or consumed by the sources (UG, PV, ES) and loads are presented as percentages of the total generated power. In the case of the commercial load demand (Fig.9), the PV generates 47% of the total power giving priority to the consumers' demand, while the rest is sold to the UG. While, in the afternoon, both the UG and ES contribute to the loads' supply especially after 4 p.m. when the energy generated from the PV is decreasing. Overall, only 1% is sold to the UG and 93% of the total energy produced is used by the consumers. On the other hand, for the domestic use profile, when the electricity price is high, the demand is low. The remained PV power (almost 12% of the total power consumed) is either sold to the UG or is used to charge the batteries (also charged during the night, when the electricity cost is lower). In general, in both cases, whenever the PV power fully covers the consumers' demand, the remaining power is either stored in the ES system or sold to the UG.

As a next step, several simulations are performed for different number of control points, N from the B−splines parametrization and the results are depicted in Table 4. We observe that as the number of control points grows, the

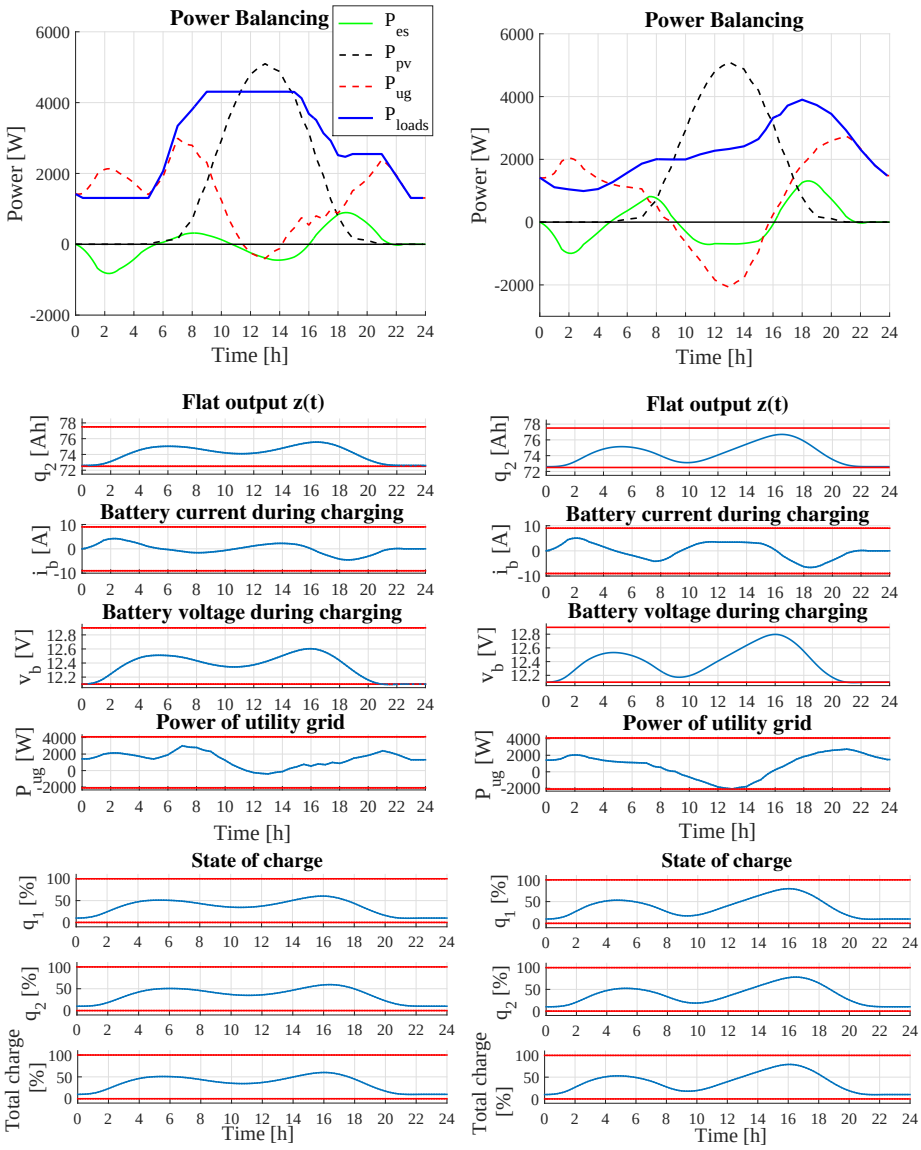

(a) (b)

Figure 9: (a) Power balancing, optimal reference profiles and state of charge of the ES system of the commercial load profile. (b) Power balancing, optimal reference profiles and state of charge of the ES system of the domestic load profile. The red lines represent the corresponding constraints.

computation time and the number of battery discharges increase, whereas the electricity cost decreases. The number of discharges influences the lifetime of

Table 3: Percentage of power with respect to the total power produced or consumed.

Load profile	Power	Power produced [%]	Power consumed [%]
Commercial	P_{ug}	46%	1% sold to the UG
	P_{es}	7%	6% for ES charging
	P_{pv}	47%	–
	P_{loads}	–	93% for load usage
Domestic	P_{ug}	40%	12% sold to the UG
	P_{es}	9%	9% for ES charging
	P_{pv}	51%	–
	P_{loads}	–	79% for load usage

Table 4: Results for different numbers of control points.

Load profile	N as in (19a),(19b)	Electricity cost [euros]	Computation time [s]	ES discharges
Commercial	18	4.090	146	2
	27	4.029	257	3
	36	3.614	514	7
	45	3.447	854	9
	54	3.226	1322	11
Domestic	18	2.534	667	2
	27	2.577	779	2
	36	2.265	1013	7
	45	2.074	1230	8
	54	1.869	1230	9

the battery meaning that a large number of discharges leads to a decrease of the battery's capacitance. This results in a reduced life for the battery and, thus to higher operational costs (necessitated by its premature replacement). Additionally, the electricity cost has been calculated in the absence of the ES

and it is equal to 4.173 *euros* for the commercial use profile and 2.644 *euros* for the domestic demand.

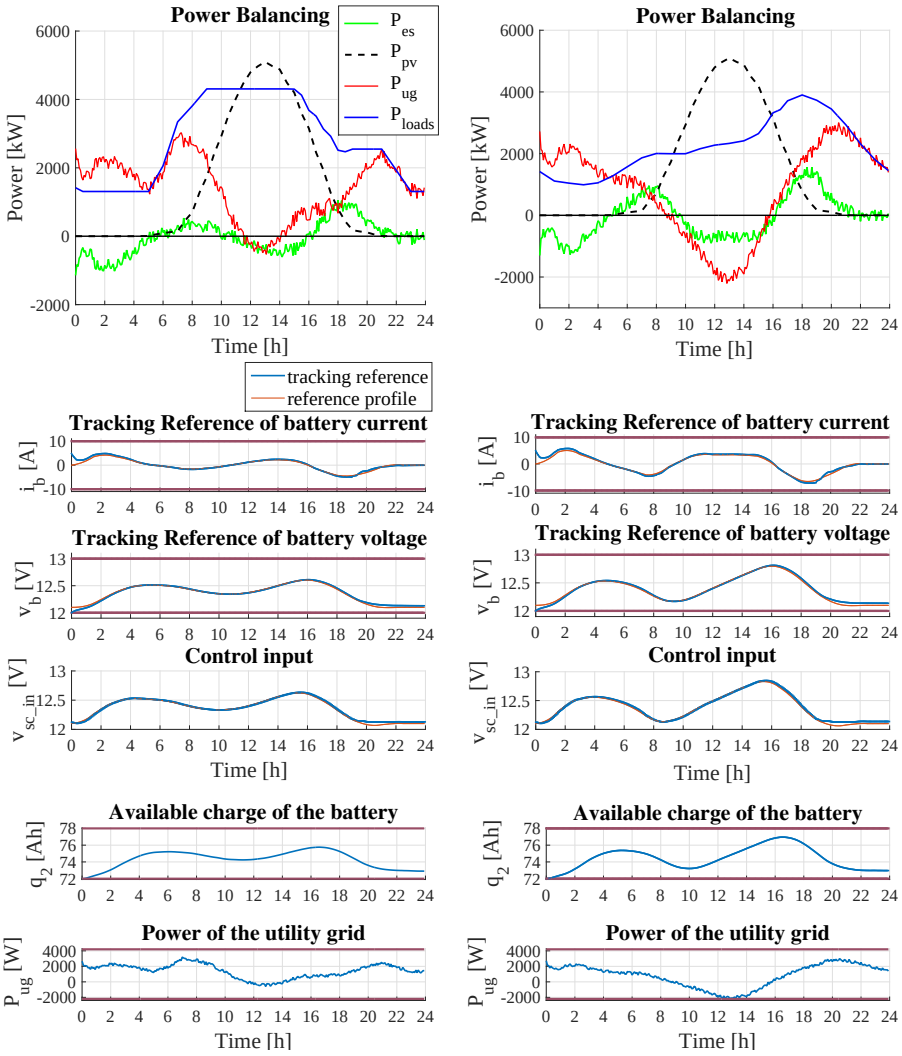

(a) (b)

Figure 10: (a) Power balancing, tracking references, available charge and UG power of the commercial load profile. (b) Power balancing, tracking references, available charge and UG power of the domestic load profile. The red lines represent the corresponding constraints.

Middle level: Afterwards, the results for the middle level are introduced using as reference the optimal profiles generated at the high level. As previously

mentioned, in the middle level, we use MPC for reference tracking with a prediction horizon, N_p, equal to 10 h and a sampling time, T_s, equal to 300 s. The power profiles of the PV and the loads are updated following the sampling time T_s. Fig.10 shows the tracking profiles of the *Power Balancing*, and the control input, v_{sc_out} (the output voltage of the Split−Pi converter, which is a function of the current, i_b, and the voltage, v_b of the battery as in (20)). According to Fig.10 and Table 5, where the power produced and the power consumed are illustrated in respect to the total power, the optimal profiles obtained at the high level are very closely followed.

Table 5: Percentage of power with respect to the total power produced or consumed. Comparison with high level optimal profiles.

Load profile	Power	Power produced [%]	Power consumed [%]	Power production difference from high level [%]	Power consumption difference from high level [%]
Commercial	P_{ug}	47%	1% sold to the UG	1%	0%
	P_{es}	6%	7% for ES charging	-1%	1%
	P_{pv}	47%	–	0%	–
	P_{loads}	–	92% for load usage	–	-1%
Domestic	P_{ug}	40%	12% sold to the UG	0%	0%
	P_{es}	9%	11% for ES charging	0%	−2%
	P_{pv}	51%	–	0%	–
	P_{loads}	–	77% for load usage	–	−2%

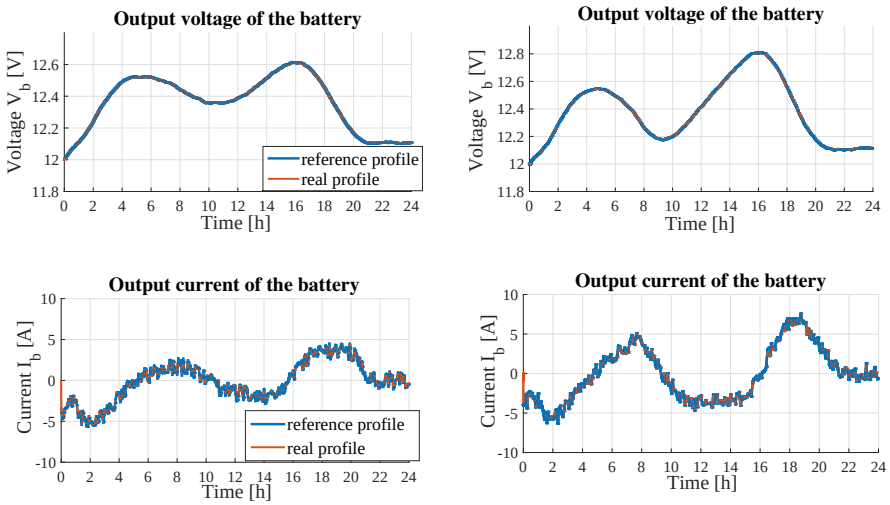

(a) (b)

Figure 11: (a) Voltage and current tracking profiles for the commercial load profile. (b) Voltage and current tracking profiles for the domestic load profile.

For the commercial load profile, a slight difference of 1% is observed in battery's charging and discharging and in the UG power production. The cost of the electricity increases at about 1% and from 4.090 raises to 4.140 *euros* for the real noise−affected profile. A similar case is also observed for the domestic load demand regarding the discharging of the battery. The computational time of the simulation lasts around 180 s for each load profile.

Low level: In the following, the results obtained at the low level are presented following the tracking profiles of the middle level for the battery current, i_b, and voltage, v_b, under perturbation (Fig.11). For the simulations, we develop the model of the ES (4, 6) in MATLAB/Simulink. The continuous−time simulation lasts about 10 s and demonstrates the proper operation of the converter which regulates very well the current and the voltage (Fig.11a, Fig.11b). The control variable d_{2sc} is updated continuously (i.e., in simulation, this means, that the values are refreshed at each simulation sampling time equal to 300 s).

Comparisons: As previously described, the reference trajectories were obtained through differential flatness and B−spline parametrization. As a next

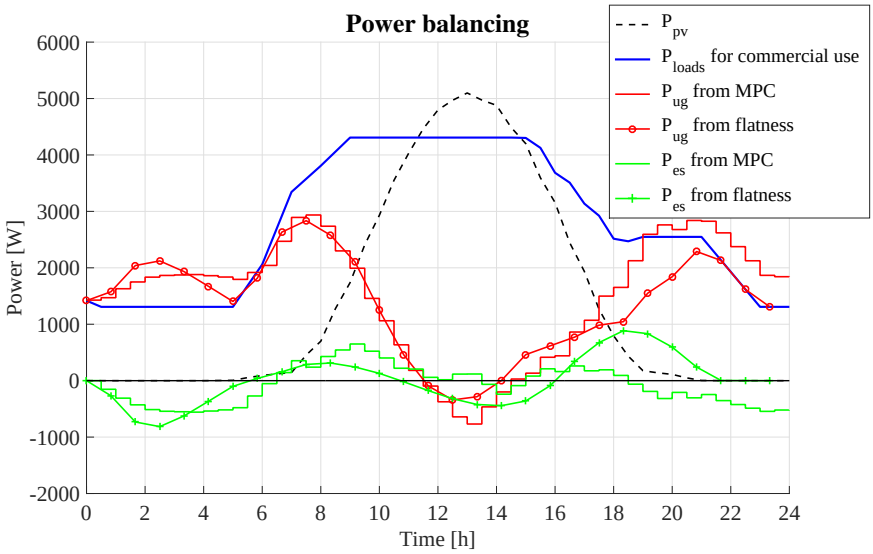

Figure 12: Power balancing using commercial load profile. Comparisons of P_{es} and P_{ug} with optimal profiles obtained by MPC.

step, the reference trajectories generation obtained through differential flatness and B−spline parametrization are compared with MPC, as presented also in [34] and [15]. The simulation results are presented in Fig.12 and Fig.14 taking into account that Np is equal to 24 h with a sampling time T_s equal to 1800 s. The obtained trajectories are similar. In Fig.13 for the commercial load profile and in Fig.15 for the domestic load profile, we take the optimal profiles generated from MPC in order to follow them directly in the low level and calculate the electricity cost. As a result, the electricity cost for the commercial use profile is equal to 4.657 *euros* and in case of the domestic use is equal to 2.912 *euros*, which is higher than the electricity cost obtained from the flatness−based optimization problem. Table 6 compares the power produced and the power consumed from the sources and loads between flatness-based approach and MPC. In both profiles with MPC, it is observed that the P_{ug} generates more power to satisfy the consumers' demand instead of exploiting the use of the battery. Consequently, although the power sold to the UG is higher with the MPC approach, the electricity cost remains higher than the electricity cost obtained from flatness as in

Table 7.

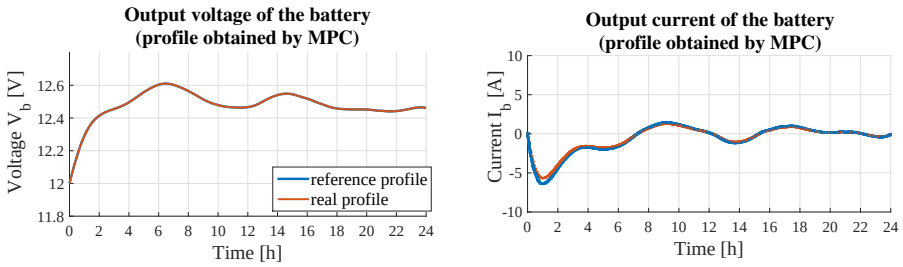

(a) (b)

Figure 13: (a) Voltage tracking profile at the low level obtained from MPC using the commercial load profile. (b) Current tracking profile at the low level obtained from MPC using the commercial load profile.

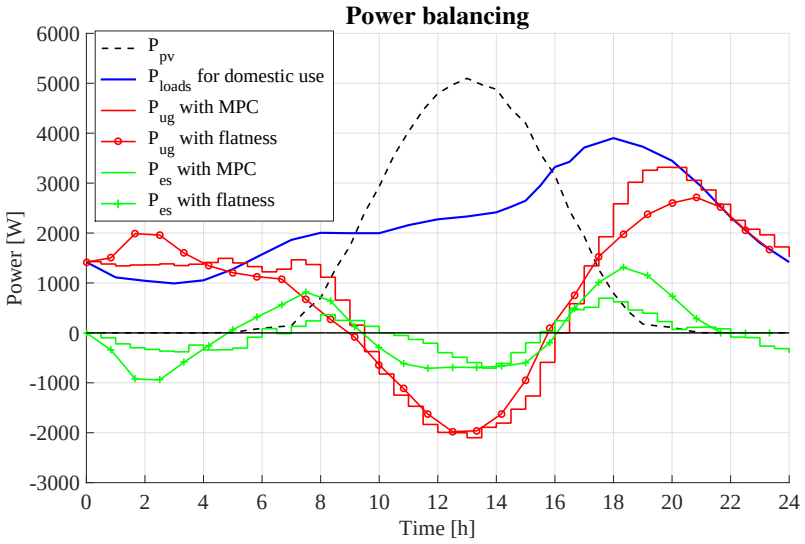

Figure 14: Power balancing using domestic load profile. Comparisons of P_{es} and P_{ug} with optimal profiles obtained by MPC.

Because of the difference in the electricity cost among the optimal profiles obtained by MPC and flatness, we perform more simulations with MPC with different prediction horizons N_p and sampling times T_s. Table 8 shows that, for MPC with a prediction horizon equal to 24 h and a sampling time equal

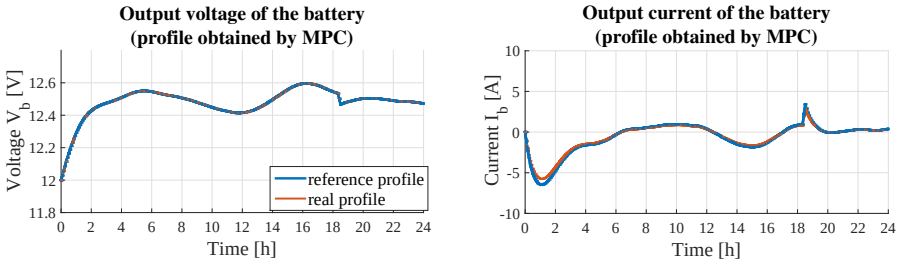

Figure 15: (a) Voltage tracking profile at the low level obtained from MPC using the domestic load profile. (b) Current tracking profile at the low level obtained from MPC using the domestic load profile.

Table 6: Percentage of power with respect to the total power produced or consumed. Comparisons with flatness-based high level Table 3.

Load profile	Power	Power produced with MPC [%]	Power consumed with MPC [%]	Power produced with flatness[%]	Power consumed with flatness[%]
Commercial	P_{ug}	49%	2% sold to the UG	46%	1% sold to the UG
	P_{es}	4%	5% for ES charging	7%	6% for ES charging
	P_{pv}	47%	–	47%	–
	P_{loads}	–	93% for load usage	–	93% for load usage
Domestic	P_{ug}	45%	14% sold to the UG	40%	12% sold to the UG
	P_{es}	4%	7% for ES charging	9%	9% for ES charging
	P_{pv}	51%	–	51%	–
	P_{loads}	–	79% for load usage	–	79% for load usage

to 1800 s, the computational time of a simulation is around 1384 s instead of approximately 150 s with differential flatness. Furthermore, because of the dis-

Table 7: Total electricity cost of the power produced from the UG and sold to the UG with MPC and flatness.

	Load profile	MPC	Flatness
Electricity cost [euros]	Commercial	4.657	4.090
	Domestic	2.912	2.534

Table 8: Simulation results obtained for optimal profiles with MPC

Load	Prediction horizon N_p [h]	Sampling time T_s [s]	Electricity cost [euros]	Calculation time [s]
Commercial	48	1800	4.416	2853
	24	1800	4.657	1384
	24	1200	4.491	1670
	24	600	4.319	1862
	10	1800	4.322	1475
	10	1200	4.281	2075
Domestic	24	1800	2.912	1868
	24	1200	2.815	2062
	10	1800	2.894	1533
	10	1200	2.889	1491
	10	600	2.774	1530

cretization in MPC, the value of the sampling time greatly influences (for better or worse) the simulation's performance (note in particular the variation of the electricity cost). Therefore, we cannot ensure which case is the most effective to obtain the optimal profiles for the optimization problem. On the other hand with differential flatness, apart from the complexity of the flat outputs' calculation to construct the objective function and constraints, there are significant advantages:

- we avoid discretization since we solve an optimization problem in continuous time;
- since the simulations generated from differential flatness with B−spline

parametrization are generated in continuous−time, the results are not affected by discretization approximations or under−sampling. Moreover, the profile is generated in its entirety for the full simulation horizon (and not piece by piece, as would be the case for a discrete optimization problem like MPC);

- practically, the total economic cost and required computational resources are lower when exploiting the flat representation.

6. Conclusion

In this paper, a multilevel supervision for a meshed DC microgrid has been introduced. Firstly, the DC microgrid system has been presented in PH form giving high importance to the ES system. Then, a constrained optimization based control approach is introduced which solves the power balancing problem. Then, the three control levels are analyzed: the high, the middle and the low level. In a meshed topology, the optimization problem to solve becomes complicated since a model consists of multiple sources, different timescales, nonlinearities and constraint satisfaction at the same time. Therefore, we built a controller that can manage and take into consideration all the aforementioned factors. Afterwards, the reference profile generation obtained with differential flatness and B−spline parametrization have been compared with the optimal profile deduced by MPC. This work has proven that the differential flatness represents an accurate and a straightforward way to purchase optimal profiles generation for power balancing optimization.

The main contributions of this work are summarized below:

- the dynamical model was given through the port−Hamiltonian formalism. This method allows a well−structured dynamical representation: it preserves power balancing relations and isolates physical quantities (such as voltage, current, charge, magnetic flux) within the model;

- the differential flatness and the associated B−splines parametrization have

been used for optimal profile generation. The method handles successfully continuous constraints (validated not only at each sampling time, but for the entire sampling interval) and integral costs (along the entire simulation horizon). Even the preliminary implementation has proven superior to a standard approach (i.e., applying MPC over a discretized model to compute the profiles iteratively);

- a multi-scale approach was implemented in the control architecture. Most of the works in the state of the art concentrate on a single aspect of microgrid control due to the large disparities in sampling times (from hours for load balancing to tenths of seconds for DC/DC converter switching). Here, each level is analyzed and an appropriate control law is given (which takes into account computation time limitations);

- overall, we may conclude that the PH implementation and the avoidance of discretization at the load balancing level provide significant improvements in comparison with standard approaches which discretize the dynamics and apply, e.g., MPC to solve the problem.

As a short term future work, further improvements in the constrained optimization problem are envisioned, e.g., energy dissipation minimization in the central transmission network by explicitly considering power losses in the cost. Furthermore, developing the transmission-line model will allow to analyze the robustness of the scheme under unexpected events, such as continuity of the system operation in case of a faulted line. In a long term future work, aspects, such as the proper sizing of the renewable sources or the batteries, addition of other elements (electrical vehicles, other battery models, other sources), will be studied. Finally, additional properties of the PH formulation will be exploited from the viewpoint of stability and performance in the control scheme (passivity, energy conservation, the Hamiltonian as a candidate Lyapunov function).

Acknowledgment

This work is funded by the French National Research Agency within the framework of the project ANR-15-CE05-004-02 $C^3\mu$ (Components, Control and Communication).

References

[1] Ahumada, C., Cárdenas, R., Saez, D., Guerrero, J. M., 2015. Secondary control strategies for frequency restoration in islanded microgrids with consideration of communication delays. IEEE Transactions on Smart Grid 7 (3), 1430–1441.

[2] Baghaee, H. R., Mirsalim, M., Gharehpetian, G. B., 2016. Performance improvement of multi-der microgrid for small-and large-signal disturbances and nonlinear loads: novel complementary control loop and fuzzy controller in a hierarchical droop-based control scheme. IEEE Systems Journal 12 (1), 444–451.

[3] Biegler, L. T., Zavala, V. M., 2009. Large-scale nonlinear programming using ipopt: An integrating framework for enterprise-wide dynamic optimization. Computers & Chemical Engineering 33 (3), 575–582.

[4] Bouzid, A. E. M., Sicard, P., Chaoui, H., Cheriti, A., Sechilariu, M., Guerrero, J. M., 2019. A novel decoupled trigonometric saturated droop controller for power sharing in islanded low-voltage microgrids. Electric Power Systems Research 168, 146–161.

[5] CIAT entreprise, U. T. C., 2014. Temperature and irradiation data. `http://www.ciat.fr/`.

[6] Cortes, C. A., Contreras, S. F., Shahidehpour, M., 2017. Microgrid topology planning for enhancing the reliability of active distribution networks. IEEE Transactions on Smart Grid 9 (6), 6369–6377.

[7] Crocker, T. R., July 2005. Power converter and method for power conversion. US Patent 6,914,420.

[8] Department of Energy Office of Energy Efficiency & Renewable Energy, E. E. R. E., 2017. Commercial and residential hourly load profiles. `https://openei.org/datasets/files/961/pub/`.

[9] Drgoňa, J., Picard, D., Kvasnica, M., Helsen, L., 2018. Approximate model predictive building control via machine learning. Applied Energy 218, 199–216.

[10] Duindam, V., Macchelli, A., Stramigioli, S., Bruyninckx, H., 2009. Modeling and control of complex physical systems: the port-Hamiltonian approach. Springer Science & Business Media.

[11] Escobar, G., van der Schaft, J., Ortega, R., 2015. A hamiltonian viewpoint in the modeling of switching power converters. Automatica 35, 445–45.

[12] Fliess, M., Lévine, J., Martin, P., Rouchon, P., 1995. Flatness and defect of non-linear systems: introductory theory and examples. International journal of control 61 (6), 1327–1361.

[13] Franke, M., Robenack, K., 2013. On the computation of flat outputs for nonlinear control systems. In: Control Conference (ECC), 2013 European. IEEE, pp. 167–172.

[14] Hernández, J., Sanchez-Sutil, F., Muñoz-Rodríguez, F., 2019. Design criteria for the optimal sizing of a hybrid energy storage system in pv household-prosumers to maximize self-consumption and self-sufficiency. Energy 186, 115827.

[15] Iovine, A., Rigaut, T., Damm, G., De Santis, E., Di Benedetto, M. D., 2018. Power management for a dc microgrid integrating renewables and storages. Control Engineering Practice.

[16] Karnopp, D. C., Margolis, D. L., Rosenberg, R. C., 2012. System dynamics: modeling, simulation, and control of mechatronic systems. John Wiley & Sons.

[17] Khan, M. R. B., Jidin, R., Pasupuleti, J., 2016. Multi-agent based distributed control architecture for microgrid energy management and optimization. Energy Conversion and Management 112, 288–307.

[18] Kofman, E., Haimovich, H., Seron, M. M., 2007. A systematic method to obtain ultimate bounds for perturbed systems. International Journal of Control 80 (2), 167–178.

[19] Kotyczka, P., Lefèvre, L., 2018. Discrete-time port-hamiltonian systems: A definition based on symplectic integration. arXiv preprint arXiv:1811.07852.

[20] Langson, W., Chryssochoos, I., Raković, S., Mayne, D. Q., 2004. Robust model predictive control using tubes. Automatica 40 (1), 125–133.

[21] Levine, J., 2009. Analysis and control of nonlinear systems: A flatness-based approach. Springer Science & Business Media.

[22] Liu, L., Meng, X., Liu, C., 2016. A review of maximum power point tracking methods of pv power system at uniform and partial shading. Renewable and Sustainable Energy Reviews 53, 1500–1507.

[23] Löfberg, J., 2004. Yalmip: A toolbox for modeling and optimization in matlab. In: Proceedings of the CACSD Conference. Vol. 3. Taipei, Taiwan.

[24] Lotfi, H., Khodaei, A., 2017. Hybrid ac/dc microgrid planning. Energy 118, 37–46.

[25] Lou, G., Gu, W., Xu, Y., Cheng, M., Liu, W., 2017. Distributed mpc-based secondary voltage control scheme for autonomous droop-controlled microgrids. IEEE Transactions on Sustainable Energy 8 (2), 792–804.

[26] Mahmoud, M. S., Hussain, S. A., Abido, M. A., 2014. Modeling and control of microgrid: An overview. Journal of the Franklin Institute 351 (5), 2822–2859.

[27] Manwell, J. F., McGowan, J. G., 1993. Lead acid battery storage model for hybrid energy systems. Solar Energy 50 (5), 399–405.

[28] Mayne, D. Q., 2014. Model predictive control: Recent developments and future promise. Automatica 50 (12), 2967–2986.

[29] Mazumder, S. K., Tahir, M., Acharya, K., 2008. Master-slave current-sharing control of a parallel dc-dc converter system over an rf communication interface. IEEE transactions on industrial electronics (1982) 55 (1), 59.

[30] Mortaz, E., Valenzuela, J., 2017. Microgrid energy scheduling using storage from electric vehicles. Electric Power Systems Research 143, 554–562.

[31] National Renewable Energy Laboratory, N. R. E. L., 2016. Rural african commercial load profile. https://www.google.com/url?sa=t&rct=j&q=&esrc=s&source=web&cd=6&ved=2ahUKEwi50M7SzMrhAhUIqxoKHX2zCg4QFjAFegQIABAC&url=https%3A%2F%2Fdata.nrel.gov%2Ffiles%2F79%2F2%2520-%2520Microgrid_Load_Profile_Explorer.xlsx&usg=AOvVaw1puui5P8p4B3DOotHUwXjv.

[32] Olaru, S., De Doná, J. A., Seron, M. M., Stoican, F., 2010. Positive invariant sets for fault tolerant multisensor control schemes. International Journal of Control 83 (12), 2622–2640.

[33] Ortega, R., Van Der Schaft, A., Maschke, B., Escobar, G., 2002. Interconnection and damping assignment passivity-based control of port-controlled hamiltonian systems. Automatica 38 (4), 585–596.

[34] Parisio, A., Rikos, E., Glielmo, L., 2014. A model predictive control approach to microgrid operation optimization. IEEE Transactions on Control Systems Technology 22 (5), 1813–1827.

[35] Parisio, A., Rikos, E., Glielmo, L., 2016. Stochastic model predictive control for economic/environmental operation management of microgrids: An experimental case study. Journal of Process Control 43, 24–37.

[36] Pham, T. H., Prodan, I., Genon-Catalot, D., Lefèvre, L., 2015. Port-hamiltonian model and load balancing for dc-microgrid lift systems. Ph.D. thesis, LCIS, Grenoble-INP.

[37] Polyuga, R. V., Van der Schaft, A., 2010. Structure preserving model reduction of port-hamiltonian systems by moment matching at infinity. Automatica 46 (4), 665–672.

[38] Prodan, I., Zio, E., 2014. A model predictive control framework for reliable microgrid energy management. International Journal of Electrical Power & Energy Systems 61, 399–409.

[39] Schiffer, J., Fridman, E., Ortega, R., Raisch, J., 2016. Stability of a class of delayed port-hamiltonian systems with application to microgrids with distributed rotational and electronic generation. Automatica 74, 71–79.

[40] Shafiee, Q., Guerrero, J. M., Vasquez, J. C., 2014. Distributed secondary control for islanded microgridsa novel approach. IEEE Transactions on power electronics 29 (2), 1018–1031.

[41] Siad, S. B., Malkawi, A., Damm, G., Lopes, L., Dol, L. G., 2019. Nonlinear control of a dc microgrid for the integration of distributed generation based on different time scales. International Journal of Electrical Power & Energy Systems 111, 93–100.

[42] Simpson-Porco, J. W., Shafiee, Q., Dörfler, F., Vasquez, J. C., Guerrero, J. M., Bullo, F., 2015. Secondary frequency and voltage control of islanded microgrids via distributed averaging. IEEE Transactions on Industrial Electronics 62 (11), 7025–7038.

[43] Stoican, F., Prodan, I., Popescu, D., Ichim, L., 2017. Constrained trajectory generation for uav systems using a b-spline parametrization. In:

Control and Automation (MED), 2017 25th Mediterranean Conference on. IEEE, pp. 613–618.

[44] Suryawan, F., 2012. Constrained trajectory generation and fault tolerant control based on differential flatness and b-splines. Ph.D. thesis, School of Electrical Engineering and Computer Science, The University of Newcastle, Australia.

[45] Takagi, T., Sugeno, M., 1985. Fuzzy identification of systems and its applications to modeling and control. IEEE transactions on systems, man, and cybernetics (1), 116–132.

[46] van der Schaft, A., Jeltsema, D., et al., 2014. Port-hamiltonian systems theory: An introductory overview. Foundations and Trends in Systems and Control 1 (2-3), 173–378.

[47] Vu, T. V., Perkins, D., Diaz, F., Gonsoulin, D., Edrington, C. S., El-Mezyani, T., 2017. Robust adaptive droop control for dc microgrids. Electric Power Systems Research 146, 95–106.

[48] Wang, B., Xian, L., Manandhar, U., Ye, J., Zhang, X., Gooi, H. B., Ukil, A., 2019. Hybrid energy storage system using bidirectional single-inductor multiple-port converter with model predictive control in dc microgrids. Electric Power Systems Research 173, 38–47.

[49] Wang, P., Lu, X., Yang, X., Wang, W., Xu, D., 2015. An improved distributed secondary control method for dc microgrids with enhanced dynamic current sharing performance. IEEE Transactions on Power Electronics 31 (9), 6658–6673.

[50] Xie, X., Yue, D., Zhang, H., Peng, C., 2017. Control synthesis of discrete-time t–s fuzzy systems: Reducing the conservatism whilst alleviating the computational burden. IEEE transactions on cybernetics 47 (9), 2480–2491.

[51] Zafeiratou, I., Nguyen, D., Prodan, I., Lefèvre, L., Piétrac, L., 2018. Flatness-based hierarchical control of a meshed dc microgrid. IFAC-PapersOnLine 51 (20), 222–227.

[52] Zafeiratou, I., Prodan, I., Lefèvre, L., Piétrac, L., 2018. Dynamical modelling of a dc microgrid using a port-hamiltonian formalism. IFAC-PapersOnLine 51 (2), 469–474.

Appendix A. Flat representation of the states and the inputs

In this part, we will present thoroughly the states and inputs of the physical model (4, 5, 6, 7) in terms of the aforementioned flat outputs and its derivatives (12c):

$$
\begin{aligned}
p_{1sc} &= \pm\sqrt{\frac{2}{g}(z_1 - \frac{h}{2}(\frac{1}{h}(\dot{z}_3+\dot{z}_2))^2 - \frac{b}{2}z_4^2)},\\
p_{2sc} &= \frac{1}{h}(\dot{z}_3+\dot{z}_2),\\
q_{1sc} &= \frac{1}{a}(\pm\frac{1}{2}\frac{1}{\sqrt{\frac{2}{g}(z_1 - \frac{h}{2}(\frac{1}{h}(\dot{z}_3+\dot{z}_2))^2 - \frac{b}{2}z_4^2)}}\frac{2}{g}(\dot{z}_1 - \frac{1}{h}(\dot{z}_2+\dot{z}_3)(\ddot{z}_2+\ddot{z}_3)-\\
&\quad - bz_4\dot{z}_4) + \frac{b}{a}z_4\cdot\cdot\frac{\dot{z}_4+(\dot{z}_2+\dot{z}_3)-(\dot{z}_2+\dot{z}_3)(1-\frac{1}{hbz_4}(\ddot{z}_3+\ddot{z}_2)}{g(\pm\sqrt{\frac{2}{g}(z_1 - \frac{h}{2}(\frac{1}{h}(\dot{z}_3+\dot{z}_2))^2 - \frac{b}{2}z_4^2)})}\\
&\quad + \frac{-\frac{c}{bz_4}(z_2 - \frac{1}{em}\dot{z}_3 - \frac{f}{e}z_3))}{g(\pm\sqrt{\frac{2}{g}(z_1 - \frac{h}{2}(\frac{1}{h}(\dot{z}_3+\dot{z}_2))^2 - \frac{b}{2}z_4^2)})},\\
q_{2sc} &= z_4,\\
q_{3sc} &= z_2 - \frac{1}{em}\dot{z}_3 - \frac{f}{e}z_3,\\
q_{1b} &= \frac{1}{em}\dot{z}_3 + \frac{f}{e}z_3,\\
q_{2b} &= z_3,\\
d_{1sc} &= 1 - \frac{\dot{z}_4+(\dot{z}_2+\dot{z}_3)-(\dot{z}_2+\dot{z}_3)(1-\frac{1}{hbz_4}(\ddot{z}_3+\ddot{z}_2)}{g(\pm\sqrt{\frac{2}{g}(z_1 - \frac{h}{2}(\frac{1}{h}(\dot{z}_3+\dot{z}_2))^2 - \frac{b}{2}z_4^2)})}+\\
&\quad + \frac{-\frac{c}{bz_4}(z_2 - \frac{1}{em}\dot{z}_3 - \frac{f}{e}z_3))}{g(\pm\sqrt{\frac{2}{g}(z_1 - \frac{h}{2}(\frac{1}{h}(\dot{z}_3+\dot{z}_2))^2 - \frac{b}{2}z_4^2)})},\\
d_{2sc} &= 1 - \frac{1}{hbz_4}(\ddot{z}_3+\ddot{z}_2) - \frac{c}{bz_4}(z_2 - \frac{1}{em}\dot{z}_3 - \frac{f}{e}z_3),\\
v_{DC} &= \frac{1}{n}\dot{q}_{1sc} + aq_{1sc} + \frac{g}{n}p_{1sc}, \qquad i_{R_{1b}} = \frac{1}{em}\ddot{z}_3 + (\frac{f}{e}+1)\dot{z}_3,
\end{aligned}
$$

where for the v_{sc}, because of the convoluted equation, we do not mention it here, but we can proceed to the calculation similarly by replacing $q_{1sc}, \dot{q}_{1sc}, p_{1sc}$ in terms of the flat outputs as it is shown above. Additionally, we consider $1/C_{1sc} = a$, $1/C_{2sc} = b$, $1/C_{3sc} = c$, $1/C_{1b} = e$, $1/C_{2b} = f$, $1/I_{1sc} = g$, $1/I_{2sc} = h$, $1/R_{1sc} = n$, $1/R_{1b} = k$, $1/R_{2b} = m$).

Appendix B. Explicit calculation of the objective function

In this appendix, we give the detailed calculations for the objective function in (15a) function of the B−splines following thee property in (18):

$$\min_{i_b(t)v_b(t)} \int_{t_0}^{t_f} \underbrace{P_{es}(t)}_{i_b(t)v_b(t)} + P_{loads}(t) - P_{pv}(t))dt = \tag{B.1a}$$

$$= \underbrace{\int_{t_0}^{t_f} e(t)(i_b(t)v_b(t))\mathrm{d}t}_{J_{es}} + \int_{t_0}^{t_f} e(t)(P_{loads}(t) - P_{pv}(t))\mathrm{d}t$$

$$\textit{subject to}: \textit{ the system dynamics } (13a) - (13k), (16a), (16b), \tag{B.1b}$$

$$v_b^{min,h} \leq \sum_{i=1}^{N} p_{\kappa_i}^{v_b} \mathcal{B}_{i,d}(t) \leq v_b^{max,h}, \tag{B.1c}$$

$$i_b^{min,h} \leq \sum_{i=1}^{N} p_{\kappa_i}^{i_b} \mathcal{B}_{i,d}(t) \leq i_b^{max,h}, \tag{B.1d}$$

$$q_{2b}^{min,h} \leq \sum_{i=1}^{N} p_i \mathcal{B}_{i,d}(t) \leq q_{2b}^{max,h}, \tag{B.1e}$$

$$P_{ug}^{min,h} \leq P_{ug} \leq P_{ug}^{max,h}. \tag{B.1f}$$

Then, we rewrite the a priori constraints from (B.1b) and (B.1f) in function of the B-splines:

$$p_{\kappa_i}^{v_b} = \frac{1}{C_{2b}} p_i + R_{2b} \left(\mathcal{P} M_{d,d-1} S_{\kappa,d-1,d}\right)_i, \tag{B.2a}$$

$$p_{\kappa_i}^{i_b} = \left(1 + \frac{C_{1b}}{C_{2b}}\right) \left(\mathcal{P} M_{d,d-1} S_{\kappa,d-1,d}\right)_i + C_{1b} R_{2b} \cdot \left(\mathcal{P} M_{d,d-2} S_{\kappa,d-2,d}\right)_i, \tag{B.2b}$$

considering (19a) and (19b). The matrices S change across the knot sub−intervals $[\tau_\kappa, \tau_{\kappa+1}]$. Thus, the constraints need to be considered for each of the intervals. For the P_{ug} constraint in (B.1f), we use the power conservation equation (10):

$$P_{ug}^{min,h} - P_{loads}(t) + P_{pv}(t) \leq P_{es}(t) \leq P_{ug}^{max,h} - P_{loads}(t) + P_{pv}(t), \quad \text{(B.3)}$$

where $P_{es}(t) = i_b(t)v_b(t)$ as aforementioned.

In the following we show also the detailed calculation of J_{es} as in (B.1a) [43]:

$$\mathcal{J}_{es} = \int_{t_0}^{t_f} e(t) \left[\frac{1}{C_{2b}} \left(\sum_{i=1}^{N} p_i \mathcal{B}_{i,d}(t) \right) + R_{2b} \left(\sum_{i=1}^{N} p_i M_{d,d-1} \mathcal{B}_{i,d-1}(t) \right) \right] \cdot \quad \text{(B.4)}$$

$$\cdot \left[\left(\frac{C_{1b}}{C_{2b}} + 1 \right) \left(\sum_{i=1}^{N} p_i M_{d,d-1} \mathcal{B}_{i,d-1}(t) \right) + C_{1b} R_{2b} \left(\sum_{i=1}^{N} p_i . M_{d,d-2} . \mathcal{B}_{i,d-2}(t) \right) \right] \mathrm{d}t$$

The previous multiplication in (B.4) concludes in 4 terms and we proceed to the calculation of the J_{es} by solving each term separately:

$$Term_1 = \left(\frac{C_{1b}}{C_{2b}^2} + \frac{1}{C_{2b}} \right) \int_{t_0}^{t_f} e(t) \left(\sum_{i=1}^{N} p_i \mathcal{B}_{i,d}(t) \right)^T \left(\sum_{j=1}^{N} \left(\mathcal{P} M_{d,d-1} \right)_j \mathcal{B}_{j,d-1}(t) \right) \mathrm{d}t =$$

$$= \left(\frac{C_{1b}}{C_{2b}^2} + \frac{1}{C_{2b}} \right) \sum_{i=1}^{N} \sum_{j=1}^{N} p_i \left(\mathcal{P} M_{d,d-1} \right)_j \int_{t_0}^{t_f} e(t) \mathcal{B}_{i,d}(t) \mathcal{B}_{j,d-1}(t) \mathrm{d}t.$$

Since the $Term_1$ results in scalar values, the obtained objective function will be in quadratic form. Similarly, we continue with the calculation of the other terms:

$$Term_2 = \frac{C_{1b} R_{2b}}{C_{2b}} \sum_{i=1}^{N} \sum_{j=1}^{N} \mathcal{P}_i \left(\mathcal{P} M_{d,d-2} \right)_j \int_{t_0}^{t_f} e(t) \cdot B_{i,d}(t) B_{j,d-2}(t) \mathrm{d}t,$$

$$Term_3 = C_{1b} R_{2b} \left(\frac{1}{C_{2b}} + \frac{1}{C_{1b}} \right) \sum_{i=1}^{N} \sum_{j=1}^{N} \left(\mathcal{P} M_{d,d-1} \right)_i \left(\mathcal{P} M_{d,d-1} \right)_j \cdot$$

$$\cdot \int_{t_0}^{t_f} e(t) B_{i,d-1}(t) \cdot B_{j,d-1}(t) \mathrm{d}t,$$

$$Term_4 = C_{1b} R_{2b}^2 \sum_{i=1}^{N} \sum_{j=1}^{N} \left(\mathcal{P} M_{d,d-1} \right)_i \left(\mathcal{P} M_{d,d-2} \right)_j \cdot \int_{t_0}^{t_f} e(t) B_{i,d-1}(t) B_{j,d-2}(t) \mathrm{d}t.$$